JGR Solid Earth

RESEARCH ARTICLE

Key Points:

- Mantle viscosity is often inferred from seismic velocity observations, which are sensitive to temperature but not water content
- We show that adding magnetotelluric observations (sensitive to water content) improves viscosity estimates
- Rock composition affects viscosity estimates through its effect on seismic velocity and electrical conductivity

Correspondence to:

F. D. C. Ramirez,
f.d.c.ramirez@geo.uio.no

Author Contributions:

Software: C. Lithgow-Bertelloni
Supervision: K. Selway, C. P. Conrad
Writing – original draft: F. D. C. Ramirez
Writing – review & editing: K. Selway, C. P. Conrad, C. Lithgow-Bertelloni

Constraining Upper Mantle Viscosity Using Temperature and Water Content Inferred From Seismic and Magnetotelluric Data

F. D. C. Ramirez[1,2] [ID], K. Selway[1,2,3] [ID], C. P. Conrad[1] [ID], and C. Lithgow-Bertelloni[4] [ID]

[1]Centre for Earth Evolution and Dynamics, University of Oslo, Oslo, Norway, [2]School of Natural Sciences, Macquarie University, Sydney, NSW, Australia, [3]Future Industries Institute, University of South Australia, Adelaide, SA, Australia, [4]Earth, Planetary, and Space Sciences, University of California, Los Angeles, Los Angeles, CA, USA

Abstract Mantle viscosity controls a variety of geodynamic processes such as glacial isostatic adjustment (GIA), but it is poorly constrained because it cannot be measured directly from geophysical measurements. Here we develop a method that calculates viscosity using empirical viscosity flow laws coupled with mantle parameters (temperature and water content) inferred from seismic and magnetotelluric (MT) observations. We find that combining geophysical constraints allows us to place significantly tighter bounds on viscosity estimates compared to using seismic or MT observations alone. In particular, electrical conductivity inferred from MT data can determine whether upper mantle minerals are hydrated, which is important for viscosity reduction. Additionally, we show that rock composition should be considered when estimating viscosity from geophysical data because composition directly affects seismic velocity and electrical conductivity. Therefore, unknown composition increases uncertainty in temperature and water content, and makes viscosity more uncertain. Furthermore, calculations that assume pure thermal control of seismic velocity may misinterpret compositional variations as temperature, producing erroneous interpretations of mantle temperature and viscosity. Stress and grain size also affect the viscosity and its associated uncertainty, particularly via their controls on deformation regime. Dislocation creep is associated with larger viscosity uncertainties than diffusion creep. Overall, mantle viscosity can be estimated best when both seismic and MT data are available and the mantle composition, grain size and stress can be estimated. Collecting additional MT data probably offers the greatest opportunity to improve geodynamic or GIA models that rely on viscosity estimates.

Plain Language Summary Many geological processes depend on the viscosity of the upper mantle, which describes how easily the rocks can "flow." The larger the viscosity of the upper mantle, the slower and/or harder it is for rocks to deform over geological timescales. Thus, constraining upper mantle viscosity would certainly help us to understand and even simulate many geodynamic processes, such as Earth's surface response to past ice melting. Although mantle viscosity cannot be measured directly, rock deformation experiments tell us how viscosity depends on rock properties, many of which can be determined from geophysical observations. Here we develop a method that calculates mantle viscosity from estimates of temperature and water content inferred from seismic and magnetotelluric (MT) observations, respectively. We show that the combination of these two observations improves viscosity estimates compared to either observation alone. When estimating viscosity from seismic and MT data, rock composition has to be considered. Because rock composition directly affects the interpretation of geophysical observations, better knowledge of rock composition can greatly reduce uncertainty in viscosity estimates. Overall, we conclude that additional MT surveying could offer new opportunities to better constrain viscosity in regions where robust geodynamic modeling is needed.

1. Introduction

Mantle viscosity controls the pace of upper mantle dynamics, including rates for plate motions, subduction deformation, small-scale convection, and glacial isostatic adjustment (GIA) processes. In particular, upper mantle viscosity influences the rate of surface uplift and associated sea level change caused by GIA, which is the viscous response of the Earth to changes in ice mass. However, surface uplift rates measured by geodesy (e.g., GNSS) in places with modern-day ice sheets such as in Greenland and Antarctica additionally measure the instantaneous elastic response of the solid earth to modern-day deglaciation (e.g., Conrad & Hager, 1997; Mitrovica et al., 2001). Thus, regional patterns of ground uplift and relative sea level (RSL) change depend on both the

instantaneous elastic and long-term viscous components (e.g., Conrad, 2013). To accurately infer rates of ice loss in polar regions (e.g., Khan et al., 2016), the elastic and viscous contributions to the surface uplift must be separated from each other. Achieving this requires a robust GIA model, which unfortunately is usually not available in polar regions because of poorly-constrained mantle viscosity. This study aims to investigate how geophysical observations (independent of geodetic observations) can be used to calculate and constrain upper mantle viscosity.

Mantle viscosity is commonly constrained from observations of GIA-induced phenomena (e.g., RSL changes over time, temporal changes in Earth's gravitational field, and polar wander feedbacks) (e.g., Kaufmann & Lambeck, 2000; Mitrovica & Forte, 1997; Peltier, 2004; Peltier et al., 1978). However, these calculations generally produce 1-D (layered) viscosity profiles defined by only a few viscosity layers due to the depth-insensitivity of GIA observables (e.g., Paulson et al., 2007) and because the ice-loading history are usually broad scale (100–1000s of km). This restricts us from inferring regional lateral variations in viscosity that may influence GIA observations (e.g., Paulson et al., 2005). Furthermore, such observations are geographically bound to places where ice history and RSL change are known. Similarly, mantle viscosities inferred from viscoelastic relaxation models for post-seismic deformation near subduction zones (e.g., Pollitz et al., 2008; K. Wang et al., 2012) are geographically constrained, data-limited, and frequency or time dependent that commonly results in lower values ($10^{17} - 10^{18}$ Pa·s) than the usual lower mantle viscosity bound (10^{19} Pa·s). Hence, other sources of information, independent from any GIA observables and seismic events, that can place additional constraints on mantle viscosity are important. For instance, localized geophysical measurements, such as seismic and magnetotelluric (MT) observations, can be used to infer variations in mantle structure that also relate to mantle viscosity (e.g., Ivins et al., 2022; Liu & Hasterok, 2016; O'Donnell et al., 2017; Selway et al., 2020). Because such geophysical measurements scan the subsurface of the Earth, they can provide good depth and lateral resolution for upper mantle structure. However, systematic methods for converting seismic and MT observations into 3-D viscosity models require more development and the uncertainties associated with such conversions are poorly constrained.

Here we investigate the relationship between the empirically-determined rheology of mantle minerals and the mantle parameters that can be observed geophysically. From rock deformation experiments, olivine rheology is thought to be controlled primarily by temperature T, water fugacity f_{H2O}, grain size d, differential stress τ, melt fraction φ, and pressure P (e.g., Bercovici & Ricard, 2012; Hirth & Kohlstedt, 1996; Karato & Jung, 2003) as described by the stress - strain rate $\dot{\epsilon}$ relationship for power law creep,

$$\dot{\epsilon} = A\tau^n d^{-p} f_{H2O}^r \exp(\alpha\varphi)\exp\left(-\frac{E^* + PV^*}{RT}\right) \tag{1}$$

where E^* is the activation energy, V^* is the activation volume, R is the ideal gas constant, and A, p, n and r are all laboratory-derived parameters (e.g., Hirth & Kohlstedt, 2003). The stress - strain rate relationship may be linear ($n \sim 1$) or non-linear ($n > 1$) if the dominant deformation mechanism is diffusion (strongly grain size sensitive) or dislocation (strongly stress sensitive) creep, respectively. In either case, we define an effective viscosity as:

$$\eta_{eff} = \frac{\tau}{\dot{\epsilon}_{tot}} \tag{2}$$

where $\dot{\epsilon}_{tot} = \dot{\epsilon}_{dis} + \dot{\epsilon}_{dif} + \dot{\epsilon}_{DisGBS}$ is the total strain rate contributed by the major plastic deformation mechanisms in olivine, here considered to be dislocation creep, diffusion creep, and dislocation-accommodated grain boundary sliding, respectively. For non-linear cases ($n > 1$), the effective viscosity is stress-dependent.

Combining Equations 1 and 2, it is clear that the effective viscosity of mantle aggregates decreases with increasing temperature, water content and melt fraction. Thus, constraining these factors from geophysical observations can improve estimates of mantle viscosity. Temperature can be estimated from seismic (e.g., Goes et al., 2000; Heeszel et al., 2016; Lucas et al., 2020; Milne et al., 2018), MT (e.g., Selway et al., 2020) and heat flow (e.g., Artemieva, 2006) data. Indeed, seismic tomography models are widely used to infer mantle thermal structure (e.g., Goes et al., 2000; Lloyd et al., 2015), with the assumption that seismic velocity anomalies are mainly thermally-controlled (e.g., Ivins & Sammis, 1995). Many such studies neglect compositional effects that can influence seismic velocity (c.f., Fullea et al., 2021; Lee, 2003; Shen et al., 2018; Xu et al., 2008). Thus, variations in chemical composition (i.e., iron, magnesium, silica and calcium content) that affect the density and elastic

moduli of the mantle rocks may be misinterpreted as thermal variations. In this case, inference of temperature from seismic observations may result in erroneous viscosity estimates.

MT images the Earth's electrical conductivity, which, in addition to being highly sensitive to temperature, is also sensitive to the presence of partial melt, conductive mineral phases and the water (hydrogen) content of nominally anhydrous minerals. Thus, the water content in nominally anhydrous olivine (as well as partial melt) can be quantified from MT if temperature is constrained (e.g., Yoshino et al., 2009). Estimates of viscosity may additionally depend on other factors such as partial melt, grain-size variations, or stresses. If present, partial melt will have a seismic and MT response (e.g., Chantel et al., 2016). By contrast, grain size in general cannot be directly inferred from geophysical observables, apart from its impact on seismic attenuation (e.g., Faul & Jackson, 2005). However, information on grain size can potentially be gained from mantle xenoliths (e.g., Ave Lallemant et al., 1980) and a region's tectonic history. The distribution of stresses can be inferred from numerical or analytical models (e.g., Johnston et al., 1998; Stevens et al., 2016) of tectonic activity or loading.

In this study, we develop a method to estimate upper mantle viscosity using a three-step process: (a) constrain temperature from seismic observations (after accounting for possible compositional variations); (b) constrain the water content from MT observations; and finally, (c) convert the calculated thermal and water content profiles into a viscosity structure using Equations 1 and 2. In each step, we assess uncertainties, particularly those associated with the geophysical observations themselves. Using this method, we expect to develop geophysically-derived mantle viscosity models that will be particularly useful in polar regions where the GIA response is poorly constrained.

2. Sources of Uncertainty in Calculating Effective Viscosity

When using Equation 2 to convert geophysical models to mantle viscosity, the main sources of uncertainty are (a) uncertainties in the geophysical observations themselves, and (b) experimental uncertainties. These experimental uncertainties can be present in the conversion of the geophysical parameters into temperature and composition, and in the calculation of effective viscosity from temperature, composition and other parameters. In this work, we are seeking to explore which parameters have the biggest impact on viscosity estimates and to provide a framework for future researchers to make viscosity calculations. Therefore, we have set depth-independent estimates for the uncertainties on the geophysical responses, as described in Section 4. Actual uncertainties on the geophysical responses will vary with geophysical setting and can be calculated by a practitioner using the framework we have provided. Incorporating estimates of the experimental uncertainties into our calculations is more complex, in part because fully characterized uncertainties and errors are often not recorded in the presentation of experimental results. Experiments are, by necessity, carried out under conditions that are simplified compared to the real Earth, and it is common that measurement uncertainties even for key parameters may not be fully explored, measured or reported. Therefore, we do not consider it possible to include experimental uncertainties in our analysis and attempting to do so would likely lead to misleading results. Care should therefore be taken when considering numeric results from our analysis and instead we focus on the comparative importance of different factors for estimating viscosity. Importance of composition and some key individual experimental conversions are also considered in more depth below.

2.1. Seismic Wave Velocity and Its Conversion to Temperature

Empirically, seismic velocity is sensitive to both temperature and composition (e.g., Lee, 2003; Shen et al., 2018). Thus, it is possible to convert the observed seismic velocity to temperature for a given bulk composition. However, in practice, conversion of seismic observations (i.e., seismic tomography) into temperature variations often neglects compositional variations, which may introduce erroneous inferences of mantle viscosity. The approximation of uniform composition is appropriate for chemically homogeneous areas of the mantle, but temperature and viscosity variations are likely in regions with strong chemical heterogeneities. Thermodynamic models (e.g., HeFESTo (Stixrude & Lithgow-Bertelloni, 2005b, 2011)) that can self-consistently predict mineral assemblages and physical properties for a given mantle lithology are a good starting point for the conversion of velocity to temperature. To further account for the possible effects of compositional heterogeneity, we consider the impact of lithological variations on seismic velocity (and thus on temperature and viscosity as well).

Seismic velocities of individual minerals can be calculated using thermodynamic relationships and extrapolations based on finite strain theory of mineral physics experimental data on elastic moduli and densities (e.g., Bina & Helffrich, 1992; Hacker & Abers, 2004; Ita & Stixrude, 1992). Mineral abundances can then be combined to compute the seismic velocity of a given bulk composition. One disadvantage of such hybrid models is that they do not self-consistently predict the stable phase assemblage for a given bulk composition at pressure and temperature, which can introduce further uncertainty into temperature inferences. Alternatively, one may use fully self-consistent approaches such as Perple_X (Connolly, 2005) or HeFESTo (Stixrude & Lithgow-Bertelloni, 2005b, 2011) that minimize the Gibbs free energy to predict the stable phase assemblage and strain derivatives of the thermodynamic potentials to predict elastic moduli and equations of state. The latter methods have the advantage of self-consistency between the phase assemblage and the physical properties and strong theoretical frameworks for extrapolations of bulk and shear moduli as a function of both pressure and temperature. For HeFESTo the most relevant approximation is bulk compositions limited to the CFMASN (CaO–FeO–MgO–Al_2O_3–SiO_2–Na_2O) system which should however capture both the most abundant species and those responsible for the vast majority of seismic heterogeneity. Minor phases related to the presence of volatiles are unlikely to affect the seismic velocities significantly or at a level comparable to other geophysical or experimental uncertainties. For this reason we separately assess the effects of volatiles on viscosity.

The principal source of uncertainty in the thermodynamic predictions stems from uncertainties in the mineral physics measurements of phase stability and physical properties at pressure and temperature. These are difficult to estimate and propagate because inter-laboratory comparisons due to pressure and temperature calibration are difficult. Given technological advances these uncertainties are likely to be smaller than those estimated by Stixrude and Lithgow-Bertelloni (2005a), which are on the order of 0.06 km/s. The spread due to the averaging scheme (Voigt-Reuss-Hill) are smaller than the experimental uncertainties (Stixrude and Lithgow-Bertelloni, 2005a, 2012). Uncertainties related to the effects of attenuation on shear-wave velocity are accounted for in our calculations as we use Q-corrected velocities, using the Q model QR19 (Romanowicz, 1995). Considering thermodynamic conversion uncertainties on the order of 0.037 km/s (from references above), translates into 100 K of temperature variation which results in approximately 1 order of magnitude viscosity variation.

2.2. Electrical Conductivity and Its Conversion to Temperature and Composition

The bulk electrical conductivity of mantle rocks is controlled by the conductivities of the constituent minerals, which are temperature dependent, and by the geometries of those minerals. In nominally anhydrous mantle silicate minerals, electrical conductivity is enhanced by the presence of hydrogen as point defects (e.g., Yoshino et al., 2009). Olivine is the most closely studied mineral, and different experimental results have suggested different magnitudes of the effect of hydrogen on olivine conductivity (e.g., D. Wang et al., 2006; Yoshino et al., 2009). As discussed by Gardés et al. (2014), this is probably partly due to uncertainties in the estimation of water content that were not fully reported in the original studies. For this reason, we have used the "unified" olivine conductivity model of Gardés et al. (2014) in this work but recognize that there are experimental uncertainties not covered by this choice. Unsurprisingly, the variety of experimental results for olivine have a larger impact on bulk conductivity if a pure olivine mantle composition is assumed. As explored by Özaydin and Selway (2020) and Naif (2018), accounting for hydrogen partitioning between minerals in a peridotitic mantle reduces the impact of different olivine experimental results on bulk mantle conductivity. Significant uncertainties in bulk conductivity are also introduced by uncertainties in the geometry of the rock and the degree of interconnectivity between different mineral phases, which is inherently poorly constrained for mantle rocks. We have used a modified, multi-phase Archie's Law to define geometry (see Section 6.2) as it is easily adaptable to a situation where the modal proportions and rock geometry are better known. For all bulk conductivity calculations, we use the software Mantle Analysis Tool for Electromagnetics (MATE, Özaydin & Selway, 2020) to construct electrical conductivity distribution for a known composition and geotherm as it allows for calculations with different compositions and experimental constraints.

2.3. Experimental Constraints on Strain Rates

Strain rate experiments are also inherently difficult due to the number of experimental parameters that must be controlled, including pressure, temperature, fugacity, and composition. Depending on the experimental setup, some of rheological parameters generally must be extrapolated from laboratory to mantle conditions. As for the

Table 1
Parameters Used in Viscosity Calculations

Deformation	A ($m^p s^{-1} MPa^{-n-r}$)	n	p	r	E^* (kJ/mol)	V^* (cm^3/mol)
Dry dislocation	1.1×10^5	3.5	–	–	530	15
Wet dislocation	1.6×10^3	3.5	–	1.2	520	22
Dry diffusion	1.5×10^{-9}	1	3	–	375	6
Wet diffusion	2.5×10^{-11}	1	3	1	375	14
DisGBS	1.288×10^{-5}	3	1	1.25	423	17.6

Note. All the parameters for dislocation and diffusion creep are taken from Hirth and Kohlstedt (2003), while dislocation-accommodated grain-boundary sliding (DisGBS) values are from Ohuchi et al. (2015). We use water fugacity f_{H2O} values in calculating strain rate by converting C_{OH} to f_{H2O} using Y.-H. Zhao et al. (2004). We multiply wet dislocation and diffusion strain rates by a factor of 3.5^r to account for Bell et al. (2003) calibration, which is accounted for by Y.-H. Zhao et al. (2004) but not by Hirth and Kohlstedt (2003).

seismic velocity and electrical conductivity experiments, the uncertainties in these parameters are not always recorded (e.g., Hirth & Kohlstedt, 2003), which makes a full assessment of the uncertainty of the experiments challenging. The reported uncertainties are generally those involved in fitting an equation to the experimental results and relying on these alone could lead to misleading implications for overall uncertainty. One significant source of experimental uncertainty in strain rate experiments is the impact of multiple mineral phases and grain sizes on bulk strain rate (e.g., Hansen & Warren, 2015). Although current experiments show that multiple mineral phases are likely to have a significant impact on bulk strain rate, only olivine has been tested extensively enough to have fully characterized flow laws. For this reason we limit our calculations to olivine flow laws presented in Hirth and Kohlstedt (2003; Table 1) but, as before, acknowledge that the magnitudes of our calculated strain rates are likely to be affected by these uncertainties and simplifications.

3. Set-Up for Constraining Effective Viscosity From Geophysical Constraints

To investigate how MT and seismic data can be used to constrain mantle viscosity, we consider a simplified, theoretical upper mantle region at depth z (e.g., target region in Figure 1a) composed of a melt-free, pure olivine. First, we forward model absolute shear wave seismic velocities V_s and electrical conductivities σ for pure olivine (Fo_{90}) at a range of temperatures T and water contents C_{OH} (Figure 1b) at fixed pressure (or depth) using the Hacker and Abers (2004) approach for V_s and the water-dependent formulation of Gardés et al. (2014) for electrical conductivity. Then, we calculate effective viscosity η_{eff} as a function of temperature and water content (Figure 1c) for a single choice of stress and grain size using Equations 1 and 2, where C_{OH} in ppm H/Si is converted into f_{H2O} (in MPa) using the Y.-H. Zhao et al. (2004) formulation. Thus, to estimate viscosity from geophysical observations, we can use seismically-derived V_s and MT-derived σ models for a region to constrain a range of T and C_{OH} using Figure 1b. Then, by combining Figures 1b and 1c, we can determine an effective viscosity range whether we consider seismics only (Section 4.1), MT only (Section 4.2), or both (Section 4.3).

The relationship between strain rate and stress, temperature, grain size, pressure and C_{OH} depends on the relative amplitudes of the different deformation mechanisms. The dominant mechanism (colored background, Figure 1c) is that with the highest strain rate (lowest viscosity), and differs for dry (defined here as $C_{OH} \leq 100$ ppm H/Si; e.g., Mei & Kohlstedt, 2000) and wet ($C_{OH} > 100$ ppm H/Si) upper mantle conditions as well as variations in the other parameters.

3.1. Absolute Seismic Velocity and Temperature

With the aid of thermodynamic analysis and laboratory-derived parameters, the absolute elastic seismic velocity of a rock at any temperature and pressure can be estimated from the seismic velocities of the constituent minerals using the Voigt-Reuss-Hill averaging scheme. For now, we do not account for compositional effects and assume a pure olivine composition for simplicity. We investigate the plausible effects of the modal mineralogy in the absolute seismic velocities in Section 6. Figure 1b shows the absolute seismic velocities calculated using the Hacker and Abers (2004) approach for pure olivine as a function of C_{OH} and T. V_s plots as vertical contours because seismic velocities are commonly not sensitive to hydrogen content, unless the water content is very large that may significantly reduce the elastic moduli of olivine (e.g., Jacobsen et al., 2008). As expected, V_s decreases with increasing temperature because of decreasing shear modulus.

3.2. Electrical Conductivity and Water Content

The mantle minerals (i.e., olivine, pyroxene, and garnet) are nominally anhydrous but can contain small amounts of water (up to a few hundreds or thousands of ppm H/Si), which can have a significant effect on the electrical conductivity because diffusing hydrogen can carry charge. As discussed in Section 2.2, the magnitude of this
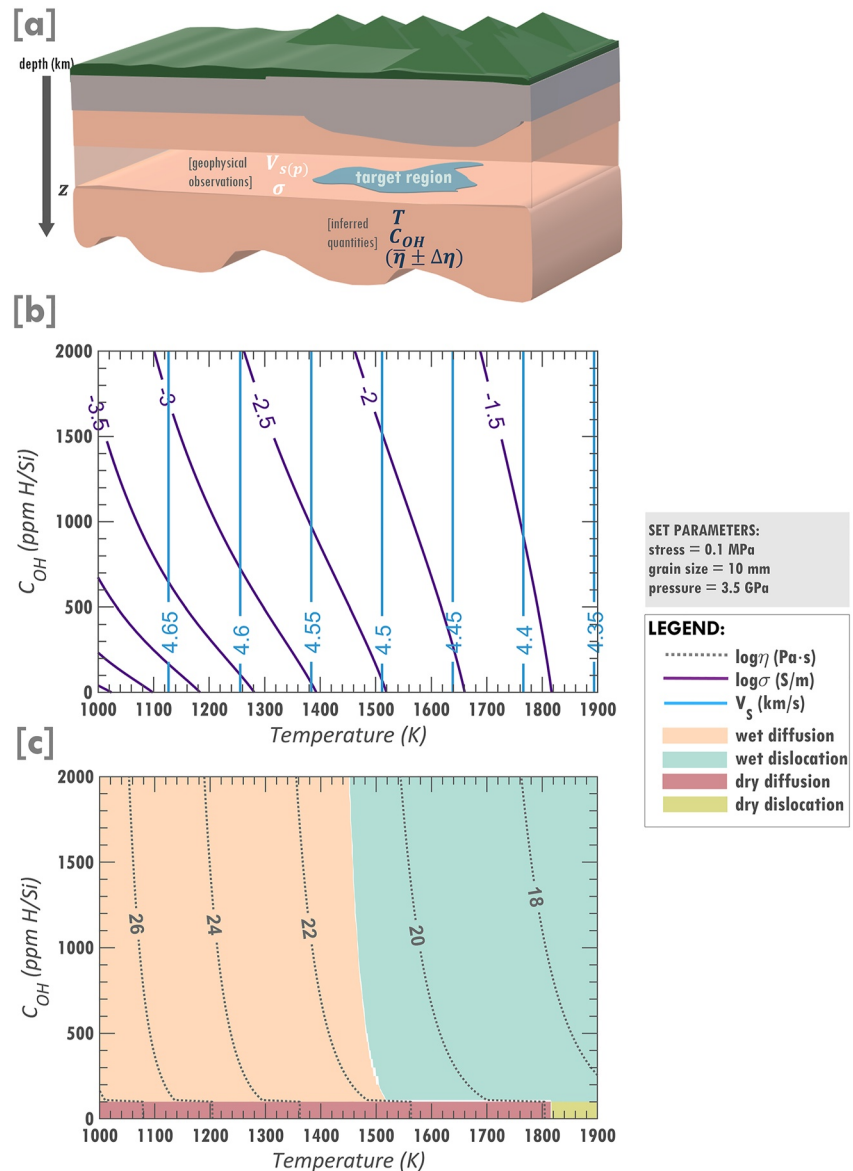
Figure 1. Inferring upper mantle viscosity from geophysical observations. (a) The set-up used in this study, where a melt-free region in the upper mantle has measured seismic velocity (V_s) and magnetotelluric-derived electrical conductivity (σ). The temperature (T) of this region is inferred from seismic velocity (neglecting compositional effects for now) and the water content (C_{OH}) is constrained from electrical conductivity if T is known. The effective viscosity is then determined by substituting the constrained T and C_{OH}, under an assumed differential stress and olivine grain size, into Equations 1 and 2. (b and c) The deformation mechanism map for pure olivine over C_{OH} and T space with shear wave velocity (blue) and electrical conductivity (violet) contour lines in panel (b), and log of effective viscosity (dotted gray) contour lines in panel (c) for a single choice of stress, grain size, and pressure. For a given geophysical observation (with uncertainty), the viscosity range can be estimated mathematically and visually by overlapping the contour lines from panel (b) onto panel (c).

effect on conductivity differs from different studies (e.g., D. Wang et al., 2006; Yoshino et al., 2009) so we utilize the unified hydrous conductivity model of Gardés et al. (2014) in calculating the total electrical conductivity (violet lines) of olivine as a function of C_{OH} and T (Figure 1b). From this, the C_{OH} for a region can be constrained if electrical conductivity is known as well as its seismically-inferred temperature range (Section 3.1).

3.3. Effective Viscosity: Estimation and Sensitivity to Controlling Parameters

The deformation mechanism map (Figure 1c), with its associated effective viscosity contour lines (dotted gray lines) can be used to (a) estimate the effective viscosity range bounded by the inferred T (Section 3.1) and C_{OH} (Section 3.2) ranges, and (b) investigate how effective viscosity varies with C_{OH} and T for different dominant deformation mechanisms. Each deformation mechanism varies differently with stress and grain size (Table 1), with diffusion creep highly sensitive to grain size, dislocation creep highly sensitive to stress, and DisGBS sensitive to both parameters, as explored in more detail in Section 5. DisGBS, which is not present in Figure 1c, becomes dominant at dry conditions under weak stresses (Section 5). Notably, moving from wet to dry conditions (Figure 1c) results in >1 order of magnitude increase in effective viscosity. This highlights the importance of constraining water content when estimating viscosity.

4. Viscosity Estimates From Geophysical Measurements

Because some uncertainty is associated with every geophysical observation, we include an estimate of this uncertainty in our calculations of viscosity from seismic (Section 4.1), MT (Section 4.2), and both seismic and MT (Section 4.3) observations. In this theoretical investigation, we make calculations with geophysical uncertainties that do not vary with depth, geotherm, physical state or composition so that we can investigate how those parameters affect viscosity uncertainty, which is our parameter of interest. For actual geophysical observations, uncertainties depend on Earth structure, composition and data quality. The uncertainties that we set are arbitrary but approximately align with common model uncertainties. For seismics, we assume an uncertainty of ± 0.05 km/s, which is the average V_s uncertainty from phase velocities at the 50–150 s period range that is sensitive to V_s structure in the lithospheric mantle and asthenosphere (Lebedev et al., 2009). For MT, we assume an electrical conductivity uncertainty of ± 0.5 log S/m, which we estimate based on the inferred conductivity ranges in Selway et al. (2019). These uncertainty ranges could also be used as a way to capture some experimental uncertainties in situations where these are known or are being investigated.

The incorporation of uncertainties in geophysical observations results in a calculated viscosity range for a region, which we visualize as a gray patch within the deformation mechanism map (Figure 2). Using this patch, we determine the range of the logarithm of the effective viscosity ($\overline{\log\eta} \pm \Delta\log\eta$), where the average of the log of effective viscosity ($\overline{\log\eta}$) and the uncertainty in the log of viscosity ($\Delta \log \eta$) are calculated by:

$$\overline{\log\eta} = \frac{(\log\eta_{max} + \log\eta_{min})}{2} \tag{3.1}$$

$$\Delta \log \eta = \frac{(\log\eta_{max} - \log\eta_{min})}{2} \tag{3.2}$$

where η_{max} and η_{min} are the maximum and minimum effective viscosities found within the patch, respectively. We determine the effective viscosity range for dry and wet upper mantle separately, to determine which viscosity law controls the overall viscosity range.

4.1. Absolute Seismic Velocity Models Only

As an example, we assume a melt-free region with an olivine grain size of 10 mm at 3.5 GPa pressure (~115 km depth) under a weak stress of 0.1 MPa. Initially, we assume that only seismic data are available and that the modeled shear wave velocity is (4.55 $\pm$ 0.05) km/s. Using the deformation mechanism map with V_s contour lines (Figure 2a), the given V_s range converts to a temperature range (red dashed lines). Since water content is not constrained by seismic data, the gray patch has the full (0–2,000 ppm H/Si) water content range resulting in a relatively large possible viscosity range, where diffusion creep is the dominant deformation mechanism for dry (≤ 100 ppm H/Si) and partly diffusion and dislocation for wet (>100 ppm H/Si) conditions. The estimated overall viscosity range as well as the separate dry and wet viscosity ranges (F2a in Figure 3a) are summarized in Table 2. As expected, the dry olivine is more viscous than the wet olivine. The associated viscosity uncertainty (Figure 3b) is smaller for slower seismic velocities (hotter regions) and larger for faster seismic velocities (colder
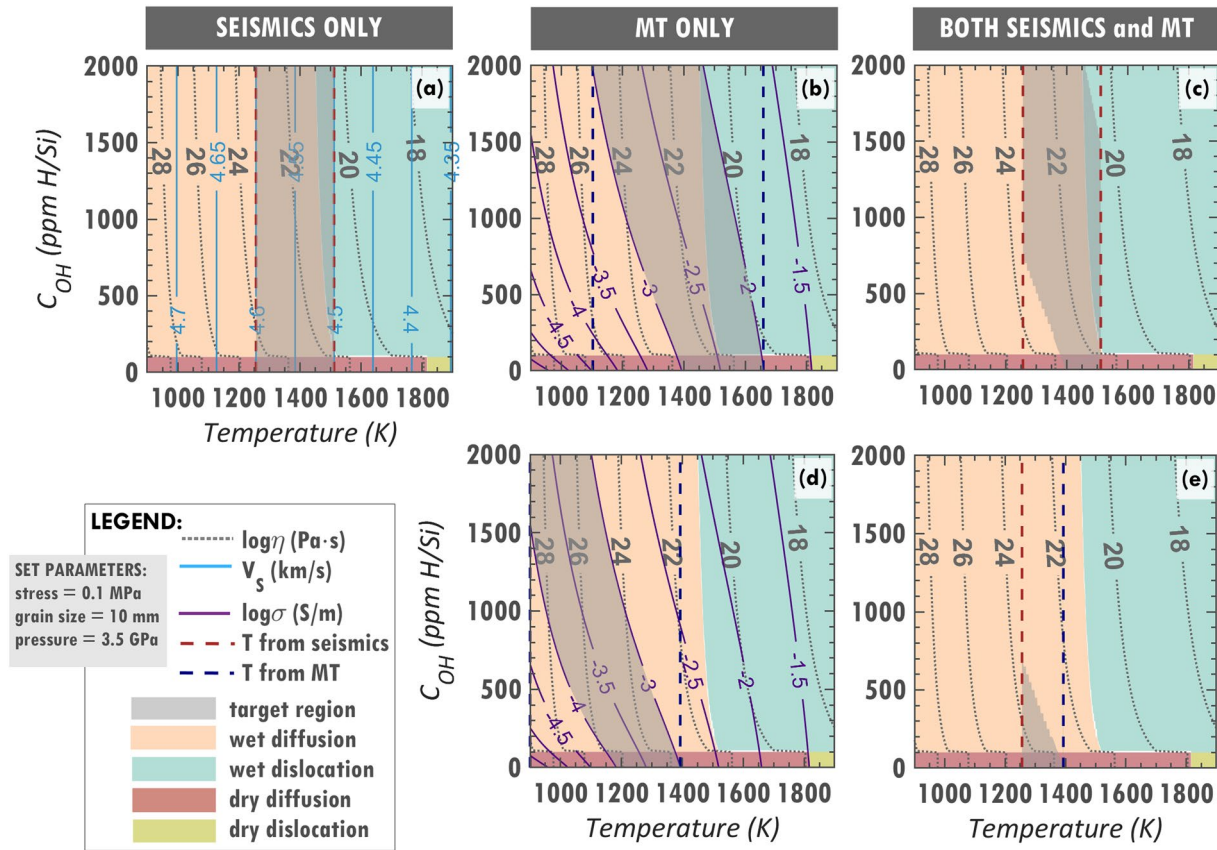
Figure 2. Estimating viscosity from (a) seismic, (b and d) magnetotelluric (MT), and (c and e) both seismic and MT constraints. The effective viscosity range for a target region with assumed geophysical observation/s (with uncertainty) is described by the minimum and maximum viscosities that fall within the gray patch. The region has an assumed $V_s = (4.55 \pm 0.05)$ km/s and $\sigma = -(2.5 \pm 0.5)$ log S/m or $-(3.5 \pm 0.5)$ log S/m. When considering only the (a) V_s or the (b and d) σ constraints, the gray patch is relatively wide, covering a large viscosity range. This viscosity range is reduced (with smaller gray patches in panels (c and e)) when both MT and seismic constraints are considered. Better constraints on viscosity are possible if there is a small overlap between seismic and MT curves (as in panel (e)).

regions) because of the non-linear temperature-dependence of viscosity. The overall viscosity has a large uncertainty of 2.5 orders of magnitude due to the unconstrained water content and the assumed V_s uncertainty.

We perform the same process to determine dry, wet and overall viscosity ranges (Figures 3a and 3b) for regions with different V_s but the same pressure, stress, grain size and V_s uncertainty. For increasing V_s (decreasing temperature), the corresponding dry, wet and overall viscosities increase both in magnitude and uncertainty. However, dry viscosity uncertainties become greater than those for wet viscosities for $V_s \geq (4.60 \pm 0.5)$km/s because the dry viscosity varies significantly across inferred low temperatures. Consistently, the calculated viscosity uncertainties are mostly greater than one order of magnitude, which indicates relatively large viscosity ranges for regions with seismic constraints only.

4.2. Electrical Conductivity Models Only

Now, we consider that the same region is instead observed using MT only, and viscosity is inferred from electrical conductivity (e.g., $10^{-(2.5\pm0.5)}$ S/m and $10^{-(3.5\pm0.5)}$ S/m in Figures 2b and 2d, respectively). Estimates of viscosity as a function of conductivity are depicted in Figure 3c for both dry and wet viscosity assumptions. If the region is more conductive (F2b in Figure 3c), the viscosity uncertainty (Figure 3d) is smaller compared to a less conductive case (F2d) because of the thermal effects on viscosity and conductivity (contours in Figure 2b). Consistently, the less conductive regions are more viscous and generally have larger viscosity uncertainties. Notably, the overall viscosities can generally be estimated from the wet viscosities, indicating that the wet viscosity laws control the overall estimates. The overall viscosity uncertainties are smaller than those with only seismic constraints. The turning point at approximately $-(3.4 \pm 0.5)$ log S/m is due to the imposed minimum temperature bound of 900 K
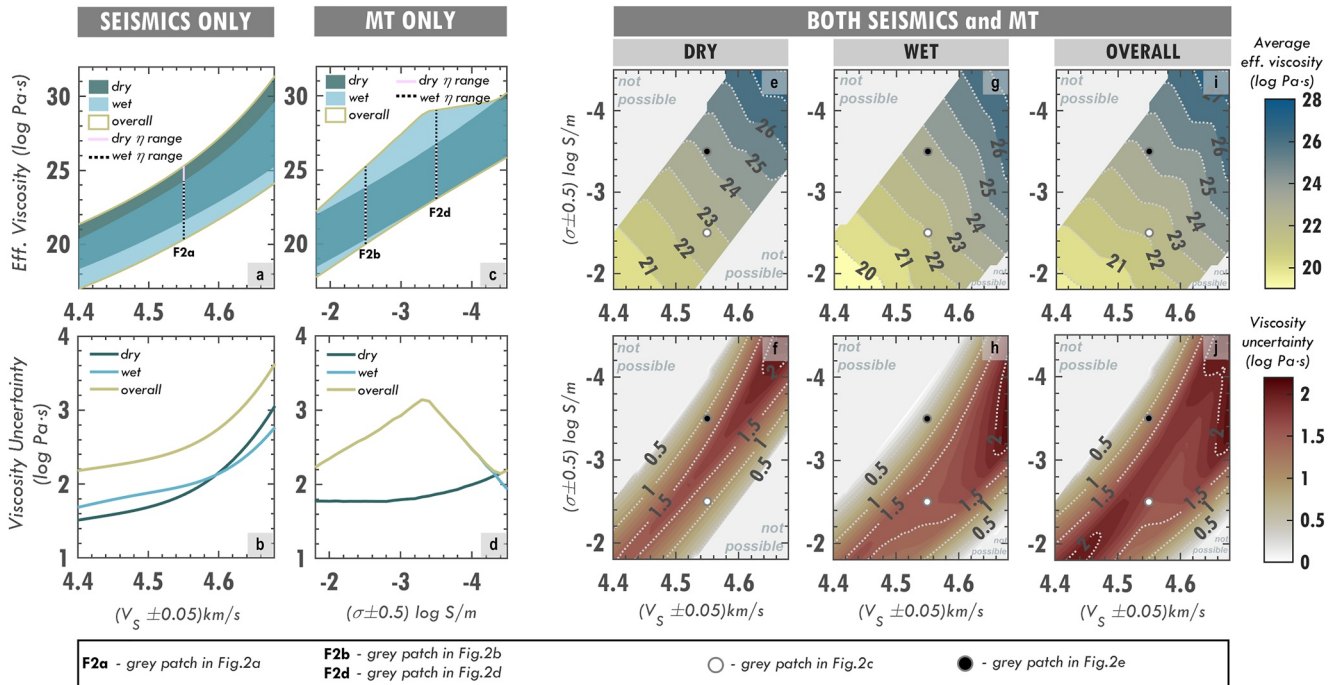
Figure 3. Viscosity estimates from geophysical observations. The effective viscosities are calculated for 10 mm olivine grain size at 3.5 GPa under 0.1 MPa stress (as in Figure 2). Dry ($\leq$100 ppm H/Si), wet (>100 ppm H/Si) and overall viscosities are estimated based on constraints from different geophysical observations. (a and c) The black dotted and pink solid lines, and (e–j) the black and white dots indicate the viscosity estimates for the sample regions in Figure 2. When both seismics and magnetotelluric (MT) are considered (e–j), viscosity uncertainties are relatively low compared to either seismics or MT alone (a–d). This uncertainty decreases as the overlap in velocity and conductivity constraints decreases (e.g., Figure 2e) until the two constraints become incompatible ("not possible" portions in panels (e–j)).

Table 2

Viscosity Estimates From Geophysical Constraints Using Different Stress-Grain Size Combinations or Ranges

Stress (MPa)	Grain size (mm)	Condition	Effective viscosity (Pa · s)		
			Seismics only	*MT only*	*Both seismics and MT*
0.1[a]	10	Dry	23.1 ± 1.9	21.8 ± 1.8	22.4 ± 1.1
		Wet	22.0 ± 2.0	22.3 ± 2.6	21.7 ± 1.6
		Overall[c]	22.5 ± 2.5	22.3 ± 2.6	21.9 ± 1.7
0.1–8[a]	1–10	Dry	20.9 ± 4.1	19.4 ± 4.1	20.2 ± 3.4
		Wet	19.7 ± 4.3	20.0 ± 4.9	19.5 ± 3.8
		Overall[c]	20.2 ± 4.8	20.0 ± 4.9	19.6 ± 4.0
5–30[b]	1–10	Dry	19.3 ± 3.9	17.4 ± 3.5	18.2 ± 2.8
		Wet	17.4 ± 3.4	18.0 ± 4.4	17.1 ± 2.9
		Overall[c]	18.6 ± 4.5	18.0 ± 4.4	17.6 ± 3.4

Note. In this example we have assumed $V_s = (4.55 \pm 0.05)$ km/s and $\sigma = -(2.5 \pm 0.5)$ log S/m as in Figures 2a–2c.

[a] Mantle convection-induced stress/es. [b] Glaciation/deglaciation-induced stresses. [c] The value encompasses both dry and wet conditions, which provides the overall viscosity, or just one of these two conditions depending on the constrained water content. Its calculated viscosity range may be the same as that of the wet or dry condition, which may indicate that (A) the region is entirely wet or entirely dry or (B) the wet and dry viscosity ranges are coincident as in Figure 3c.

which forces regions with lower conductivities to have lower water contents (left side of Figure 2d) and (artificially) smaller uncertainties. The viscosity uncertainties are mostly greater than 1.5 order of magnitude, which indicates relatively large viscosity ranges for the regions with MT constraints only.

4.3. Both Seismic and Electrical Conductivity Models

Next, we assume that the region has both seismic and MT measurements (Figures 2c and 2e). We use the seismically-determined temperature range to constrain the water content range from the electrical conductivity curve. Visually, we can simply overlay the gray patches in "Seismics Only" and "MT Only" cases. This overlap results in the gray patch for "Both seismics and MT" case which is smaller than the patches in the former cases. Consequently, their dry, wet and overall viscosities have reduced viscosity uncertainties (white and black dots in Figures 3e–3j). When one geophysical observation (either MT or seismics) estimates lower temperatures (e.g., Figure 2a dry) and the other observation estimates higher temperatures (Figure 2b dry), the combined patch is for intermediate temperatures (Figure 2c dry). However, when the patches from both MT and seismics indicate similar temperatures or one patch lies within the other patch, the use of both constraints may not significantly improve the viscosity uncertainty (e.g., white dot in Figure 3h). In contrast, we can obtain better constraints on viscosity (black dots in Figure 3) for regions where electrical conductivity and seismic curves do not overlap much, and in this case MT improves the temperature estimates.

5. Complexities From Stress and Grain Size

Here we investigate how changing the stress and grain size affects the viscosity and the associated uncertainty for the region of interest. In this study, we consider 1–10 mm grain sizes (e.g., Ave Lallemant et al., 1980) and lithospheric stresses of 0.1–100 MPa (Figure 4), where stresses ≤8 MPa are typically associated with mantle convection (Conrad & Lithgow-Bertelloni, 2006) and stresses ≤30 MPa are associated with glaciation (e.g., Johnston et al., 1998).

5.1. Large Stresses and Big Grain Sizes: Dislocation Creep Domain

The inferred effective viscosity and the associated uncertainties for a melt-free region under large stresses (>10 MPa, Figure 4) do not vary significantly with grain size. For these large stresses, the dominant deformation mechanism is dislocation creep, which is grain size independent but strongly stress dependent. This dislocation creep domain extends down to relatively weak stresses (≤1 MPa) but only for olivine grain sizes of at least 3 mm, depending on whether the region is dry (Figure 4a) or wet (Figure 4b).

5.2. Weak Stresses and Small Grain Sizes: Diffusion Creep Domain

For weak stresses (≤1 MPa, Figure 4), the average effective viscosities and the associated uncertainties vary with grain size and diffusion creep is the most important mechanism across 1–10 mm grain sizes. Within the diffusion creep domain, the average effective viscosity does not change with stress but is instead sensitive to grain size. The inferred viscosity uncertainties for weak stresses in the diffusion creep domain are smaller than those for stresses in the dislocation creep domain. This emphasizes the importance of the deformation mechanism, which is controlled by stress and grain size, when estimating viscosity and its uncertainty.

### 5.3. Intermediate Stresses: Transition Between Diffusion and Dislocation Domains

For intermediate grain sizes and stresses, multiple deformation mechanisms may function together (brown, gray and stone blue regions, Figure 4) which we describe here as transition regimes. These transition regimes are defined as those where the gray patches calculated from the geophysical responses (Figure 2) overlie more than one dominant deformation mechanism. Consequently, the average viscosities and uncertainties become sensitive to both stress and grain size and vary more rapidly than when one regime dominates, particularly in wet conditions (brown regions, Figure 4b). For the dry "Seismics Only" case, DisGBS also contributes to deformation at intermediate stresses (1–10 MPa).

### 5.4. Viscosity Estimates Using Stress and Grain Size Ranges

Since stress and grain size are often unknown, we consider a range for these parameters within Figure 4. Clearly, considering ranges for stress and grain size increases the viscosity uncertainty compared to just considering a single choice (as in Figure 2). This increase in viscosity uncertainty is greatly affected by the deformation mechanism(s) functioning in the region of interest. The dry and wet upper mantle under mantle convection stresses (0.1–8 MPa) over 1–10 mm grain sizes in Figure 4 have more combinations of possible deformation mechanisms than those under higher, glaciation-induced stresses (8–30 MPa). Notably, this complexity results in relatively large viscosity uncertainties for mantle convection stresses (Table 2), where viscosity is strongly controlled by both stress (dislocation creep and DisGBS) and grain size (diffusion creep and DisGBS).

6. The Effect of Bulk Composition on Geophysical Constraints

We expect heterogeneity in bulk composition of the upper mantle, and this is important because different rock compositions have different electrical conductivities and seismic velocities affected by variability in silica, iron and calcium content, and modal mineralogy (e.g., Karato & Karki, 2001; Xu et al., 2008). Many of the studies do not account for compositional effects on seismic velocities, particularly those inferring thermal structure based on thermodynamic conversions, because the bulk composition has to be known. Thus, seismic velocity variations, often attributed solely to temperature variations (e.g., Goes et al., 2000; Heeszel et al., 2016; Lucas et al., 2020; Milne et al., 2018), may also be due to variations in rock composition. This affects our interpretation of observed
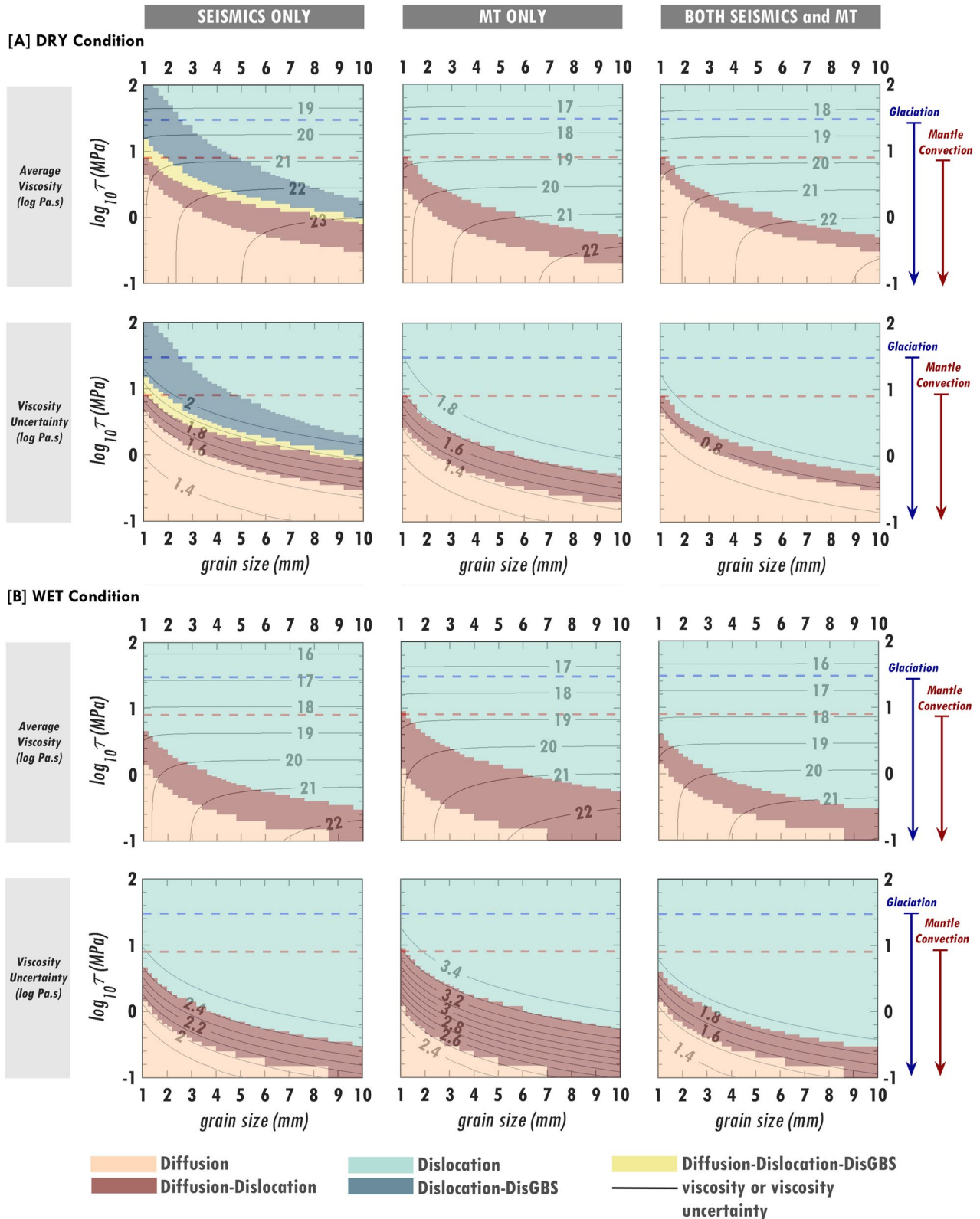
Figure 4. Viscosity estimates across stress and grain size space for (a) dry and (b) wet conditions. Shown are viscosity ranges (average viscosities and uncertainties) for a region with the same assumed geophysical constraint/s as in Figures 2a–2c, calculated for different stress and grain size combinations. The dominant deformation mechanisms are plotted as colored regions (legend), and indicate controls on viscosity and its dependence on stress and grain size (primary controllers for the deformation mechanism).
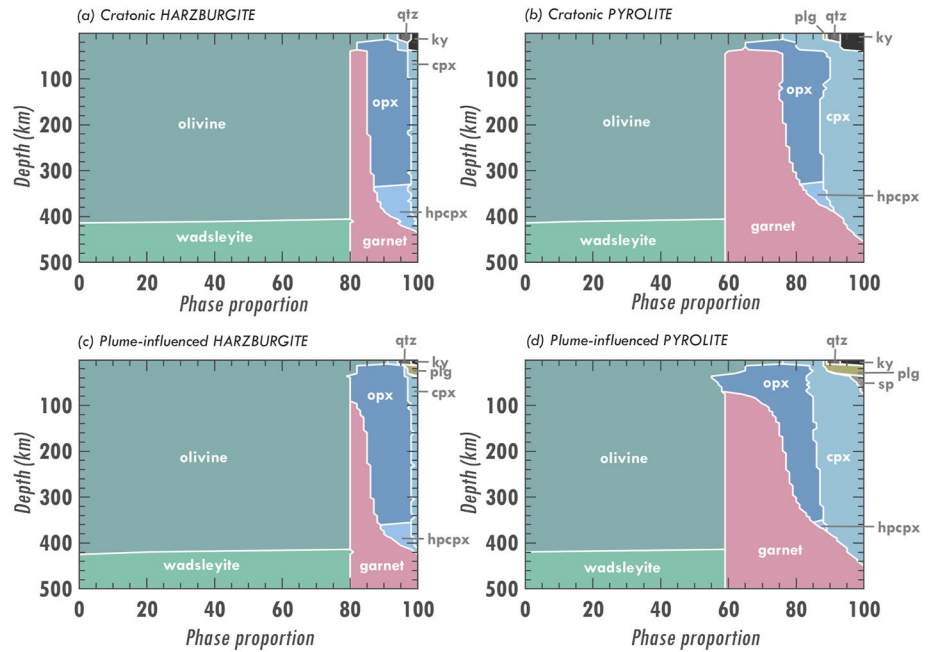
Figure 5. Phase proportions of (a and c) harzburgite and (b and d) pyrolite with (a and b) cratonic (colder, Figure 6c) and (c and d) plume-influenced (hotter, Figure 6c) geotherms. Phases are: plagioclase (plg), spinel (sp), quartz (qtz), kyanite (ky), orthopyroxne (opx), clinopyroxene (cpx), high-pressure Mg-rich clinopyroxene (hpcpx), garnet (gt), olivine (ol), and wadsleyite (wa). Computed with HeFESTo (Stixrude & Lithgow-Bertelloni, 2011) using the bulk compositions from Xu et al. (2008).

variations in seismic velocity and adds additional uncertainty when converting seismic velocity into temperature and viscosity. In addition, different minerals in mantle rock have different conductivities, and bulk conductivity is also affected by mantle temperature, water content of different minerals, water partitioning between the minerals and interconnectivity of the different phases (e.g., Özaydin & Selway, 2020), which adds additional uncertainty into our viscosity calculations.

6.1. Seismic Velocities for Different Compositions and Geotherms

Using the bulk compositions for pyrolite and harzburgite in Xu et al. (2008), we compute the stable phase assemblages at given pressure-temperature (P-T) conditions (Figure 5) as well as the corresponding seismic velocities (Figure 6a) using the self-consistent thermodynamic formalism (HeFESTo) of Stixrude and Lithgow-Bertelloni (2005b, 2011) for each of the geotherms (Figure 6c). The modeled V_S are corrected for attenuation using the seismic attenuation model QR19 (Romanowicz, 1995), where attenuation is strongest at shallower upper mantle depths (100–250 km) and then decreases at greater depths. Attenuation affects measured seismic wave speeds and will therefore impact our viscosity interpretations. Attenuation is often challenging to measure directly (e.g., Dalton & Ekström, 2006; Dalton et al., 2008) but is intrinsically linked to viscosity because deformation processes at the grain scale will also anelastically absorb seismic energy. We consider pyrolite and harzburgite here because they are geologically common and have distinct physical properties at the same pressure and temperature conditions (Figure 6a). We construct models for the geotherm (Figure 6c) based on a cold cratonic environment (blue line) and a warmer plume-influenced environment (red line). Each geotherm grades from a surface temperature of $T_0 = 0°$ to a mantle adiabat at the base of the lithosphere at 150 and 80 km depth for the cratonic and plume-influenced environments, respectively (details in Appendix). The cratonic mantle potential temperature is 1623 K and the adiabat is 0.4 K/km and the plume-influenced geotherm is assumed to have an excess mantle potential temperature of approximately 100 K with respect to the cratonic geotherm, which agrees with the observations for many plumes (e.g., Courtier et al., 2007). The parameters in all models are chosen based on common geophysical observations such as surface heat flux.
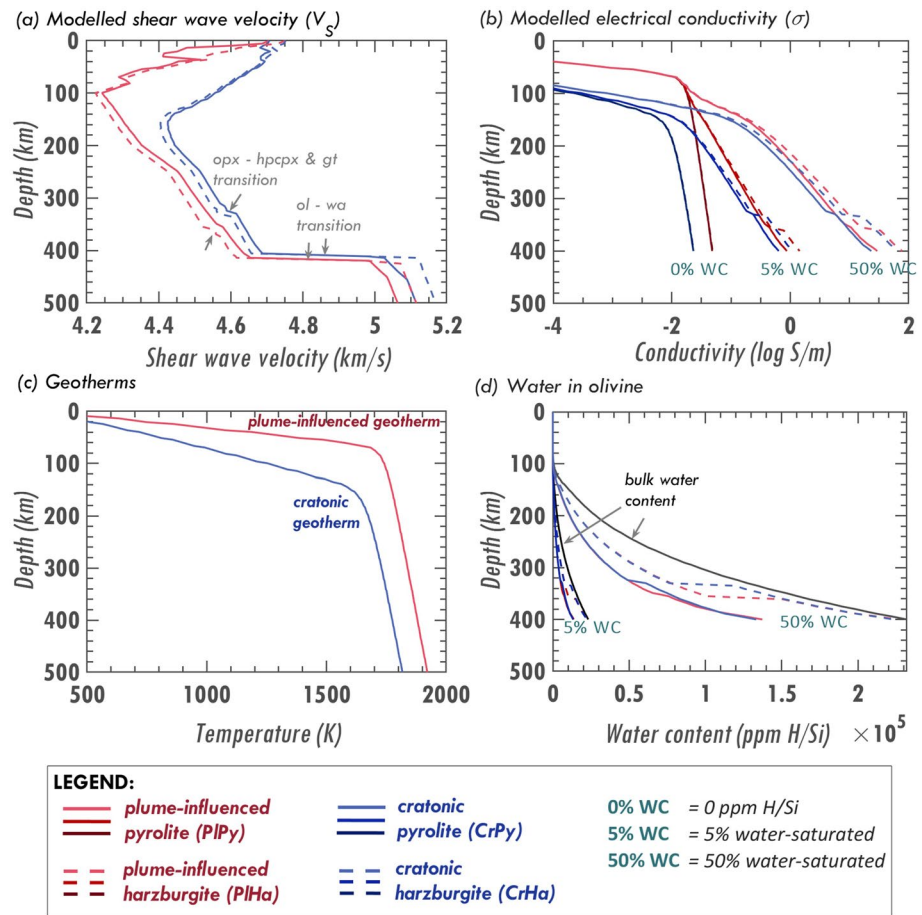
Figure 6. Modeled (a) shear wave velocities V_S and (b) electrical conductivities σ for pyrolite (solid lines) and harzburgite (dashed lines) for (c) cratonic (blue lines) and plume-influenced (red lines) geotherms. (a) The V_S trends of the compositions in Figure 5 are calculated using HeFESTo (Stixrude & Lithgow-Bertelloni, 2005b), and are corrected for attenuation. The gray arrows indicate phase transitions (see Figure 5). (b) The forward modeled bulk σ for compositions in Figure 5 at different bulk water content: 0 ppm H/Si (darkest lines), 5% water saturation (medium lines) and 50% water saturation (palest lines) using Mantle Analysis Tool for Electromagnetics (MATE) software. Water saturation of the rock is quantified as the water solubility of olivine based on the Padrón-Navarta and Hermann (2017) formulation. (d) MATE calculation of water in olivine (blue and red lines) for different compositions and geotherms from the given bulk water content (5%, black line or 50%, gray line) based on the used partitioning coefficients.

Phase proportions vary significantly with bulk composition, and less with temperature, except at shallow depths (Figure 5a). The difference in olivine, garnet and orthopyroxene modal mineralogy between harzburgite and pyrolite at the same geotherm results in a seismic velocity difference of ∼0.02–0.05 km/s below 150 km depth (Figure 6a). For the same composition but different geotherm, a seismic velocity variation of ∼0.05–0.10 km/s is mainly due to the thermal difference (∼100 K), not from the minimal change in garnet and orthopyroxene proportions (e.g., Figures 5a and 5c). Moreover, the low velocity zone (LVZ) for the plume-influenced environment occurs at shallower depths with lower minimum velocity than for the cratonic environment. In our modeled scenarios, the phase transition from olivine to wadsleyite occurs at slightly different depths and with different V_S ranges due to the combined effects of temperature and composition. Clearly, seismic velocity is dependent on both temperature and composition, and variations in both of these parameters result in seismic velocity anomalies.

6.2. Electrical Conductivities for Different Compositions and Geotherms

The bulk conductivity of a mantle rock is controlled by its temperature, modal mineralogy, bulk water content, water partitioning, interconnectivity and conductivity of the individual phases. To see how the bulk conductivity varies for different compositions, we forward model the overall conductivities for harzburgite and pyrolite

using the MATE software (Özaydin & Selway, 2020). We use the geotherms in Figure 6c and modal mineralogy in Figure 5. We use a modified Archie's law to define the rock geometry and assume that olivine is perfectly connected ($m \leq 1$, as dynamically calculated in MATE), that abundant pyroxene (10%–15%) is well connected ($m = 2$, prescribed) and that other minerals are poorly connected ($m = 4$, prescribed), where m is the Archie's law connection exponent (Glover, 2010). Estimation of the m parameter for pyroxenes and other phases is necessary because the interconnectivity of the phases and the individual phase conductivities are unknown and unconstrained. We assume different bulk water contents to see how water affects both the electrical conductivity (Figure 6c) and the viscosity estimates from MT constraints for pyrolite and harzburgite (Section 7). We consider three conditions that describe the different bulk water content: completely dry (0% WC), 5% water-saturated (5% WC), and 50% water-saturated (50% WC) mantle rocks. We define olivine water saturation from the formulation of Padrón-Navarta and Hermann (2017) since these experiments were carried out at sub-solidus conditions and we assume a melt-free mantle. From this calculation of olivine water content at saturation, we simply take fractions at 5% and 50% to determine the water contents stated above. Using the partition coefficients from the chosen models summarized in Table A1 (Appendix), we calculate the water contents of the other phases.

The composition with higher bulk water content (50% WC) is significantly more conductive than the 5% WC or 0% WC compositions (Figure 6b). For each bulk water content, the composition with the plume-influenced (hotter) geotherm is consistently more conductive than the cratonic (colder) composition. These indicate the sensitivity of conductivity to both water and temperature. In contrast, modal mineralogy has a smaller impact on the overall conductivity as seen from the minimal conductivity difference between harzburgite (dashed lines) and pyrolite (solid lines) but becomes more significant when more water is involved. Since bulk water in a mantle rock is partitioned across the constituent phases based on their individual partition coefficients, the water contents of individual minerals may change for different compositions at different bulk water contents. Consistently, olivine in harzburgite contains more water than olivine in pyrolite (Figure 6d) because more water in pyrolite has been partitioned to the pyroxene phases. Because of this extra water, we expect harzburgite to be less viscous than pyrolite for the same geotherm. This example also illustrates how the impact of experimental uncertainties can be complex and potentially case-specific, since the uncertainties related to hydrous olivine conductivity will be more important for viscosity estimation for harzburgite than for pyrolite.

6.3. Effect of Composition on Viscosity Estimates From Seismic Velocity Models

We forward modeled dry and wet viscosity structures (Figure 7) from modeled V_s profiles of the cratonic harzburgite and plume-influenced pyrolite using the method described in Sections 3.1 and 4. As before, we add a constant velocity uncertainty of ± 0.05 km/s for each V_s profile (Figure 7a) and calculate the temperatures for each composition (Figure 7b), assuming that the uncertainty for V_s is associated with uncertainties in temperature. The inferred temperatures are used in the viscosity calculation for both dry (≤ 100 ppm H/Si) and wet (> 100 ppm H/Si) conditions.

The uncertainty in the interpreted thermal structure is smaller at depths shallower than ~250 km than at greater depths, which results in more tightly constrained dry (Figure 7c) and wet (Figure 7d) viscosity structures. This implies that attenuation, which is stronger at shallower upper mantle depths, clearly influences viscosity estimates.

Compositional and thermal effects on seismic velocities may offset each other. In our models, this results in partially overlapping seismic velocities of colder cratonic harzburgite and hotter plume-influenced pyrolite at depths below ~200 km (Figure 7a). However, because we interpret these models with their known compositions, the inferred thermal and viscosity structures of the two models are different. If we were to assume that seismic velocity is dominantly temperature dependent, we would interpret that the velocity overlap at these depths implies that the regions have the same temperature and viscosity. This erroneous interpretation highlights the limitation of this assumption and demonstrates that we need to account for compositional variations when inferring thermal and viscous properties from seismic data.

For most depths, the plume-influenced pyrolite has a larger temperature range than the cratonic harzburgite. At depths where we observe large portion of overlapping V_s, there are kinks on the lower temperature bounds for both harzburgite and pyrolite caused by phase transitions (orthopyroxene to garnet (opx-gt) and orthopyroxene to high pressure magnesium-rich clinopyroxene (opx-hpcpx), Figures 5 and 6a). At these phase transitions, seismic
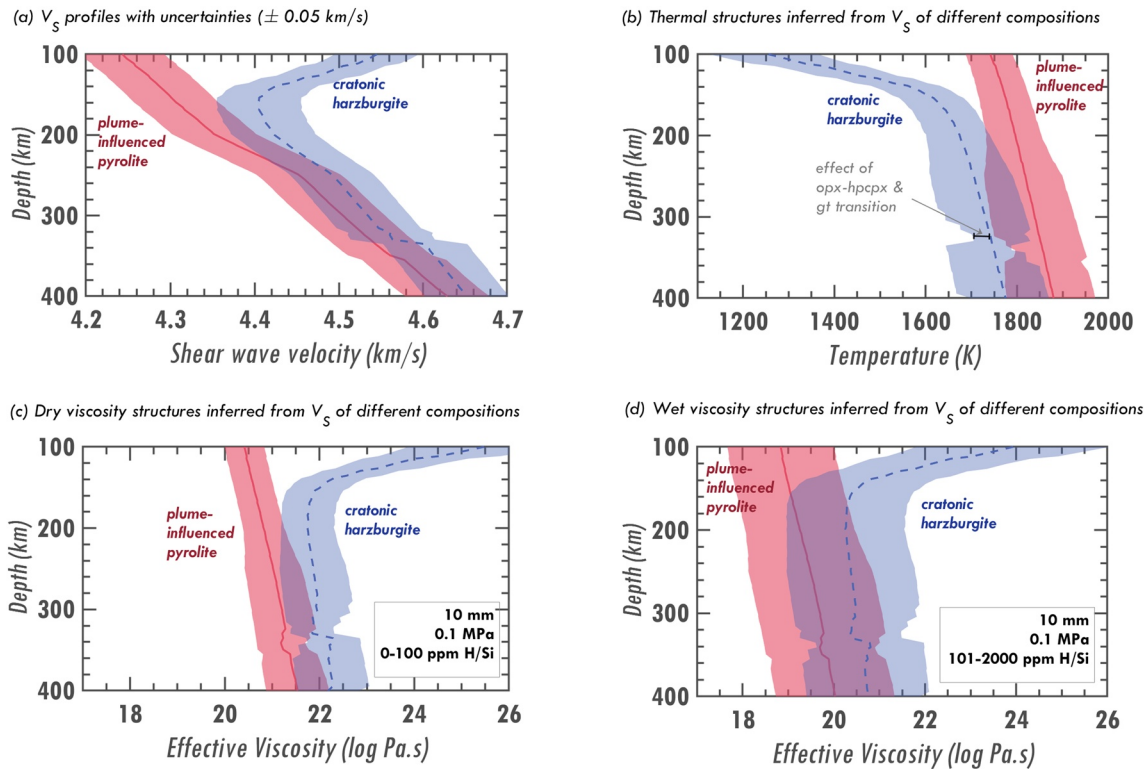
Figure 7. Constructing viscosity structures from shear wave velocities. (a) Shear wave velocity structures with constant uncertainty for plume-influenced pyrolite (pink band) and cratonic harzburgite (blue band). Partial overlap of both velocity structures occurs due to the applied velocity uncertainty. (b) The thermal structures inferred from the V_s structures in panel (a). At depths where kinks are present, the lower bound temperatures of pyrolite and harzburgite increase and become closer to the average temperatures (black segment) because of the phase transitions (opx-hpcpx and opx-gt) that occur at these temperatures and depths. (c) Dry and (d) wet viscosities calculated using the method of Section 4, which mainly uses seismically-inferred temperatures in panel (b) and unconstrained water content ranges for dry (≤100 ppm H/Si) and wet (>100 ppm H/Si) conditions. Note that the observed velocity overlaps do not correspond perfectly to the thermal and viscosity overlaps.

velocity changes significantly with a small change in temperature, which reduces the uncertainty in temperature. Thus, the phase transition also affects the viscosity estimates.

7. Applying the Method

Here we consider the reality for a practitioner attempting to estimate mantle viscosity from geophysical and other available data. We consider, from the method that we have presented, how precisely and accurately mantle viscosity can be calculated and which are the key parameters that can affect the uncertainty of that viscosity estimate. To do this, we first forward model synthetic viscosity structures assuming that we know all the important parameters, namely the compositions (harzburgite and pyrolite), geotherms, water contents, stresses and grain sizes (Figures 8a–8c). We also calculate the geophysical observations (with uncertainty) that we would expect from these physical conditions and we produce additional synthetic viscosity forward models from the geophysical data (Figures 9a–9c). We then compare the two viscosity estimates and discuss the impact of composition, water content, geophysical observations, and geophysical uncertainties when constraining viscosity estimates. There is some circularity in the comparison between these viscosity estimates because the two methods depend on some of the same experimental data and assumptions, such as the impact of temperature and water content on viscosity. For this reason, quantitative calculations of the accuracy of the viscosity estimates should be considered with caution. However, this approach allows us to investigate the situations in which different geophysical data will enable us to better estimate viscosity and also to consider how parameters such as grain size and stress, which are important in the synthetic viscosity calculations but not easily measured geophysically, will affect viscosity estimates in practice.
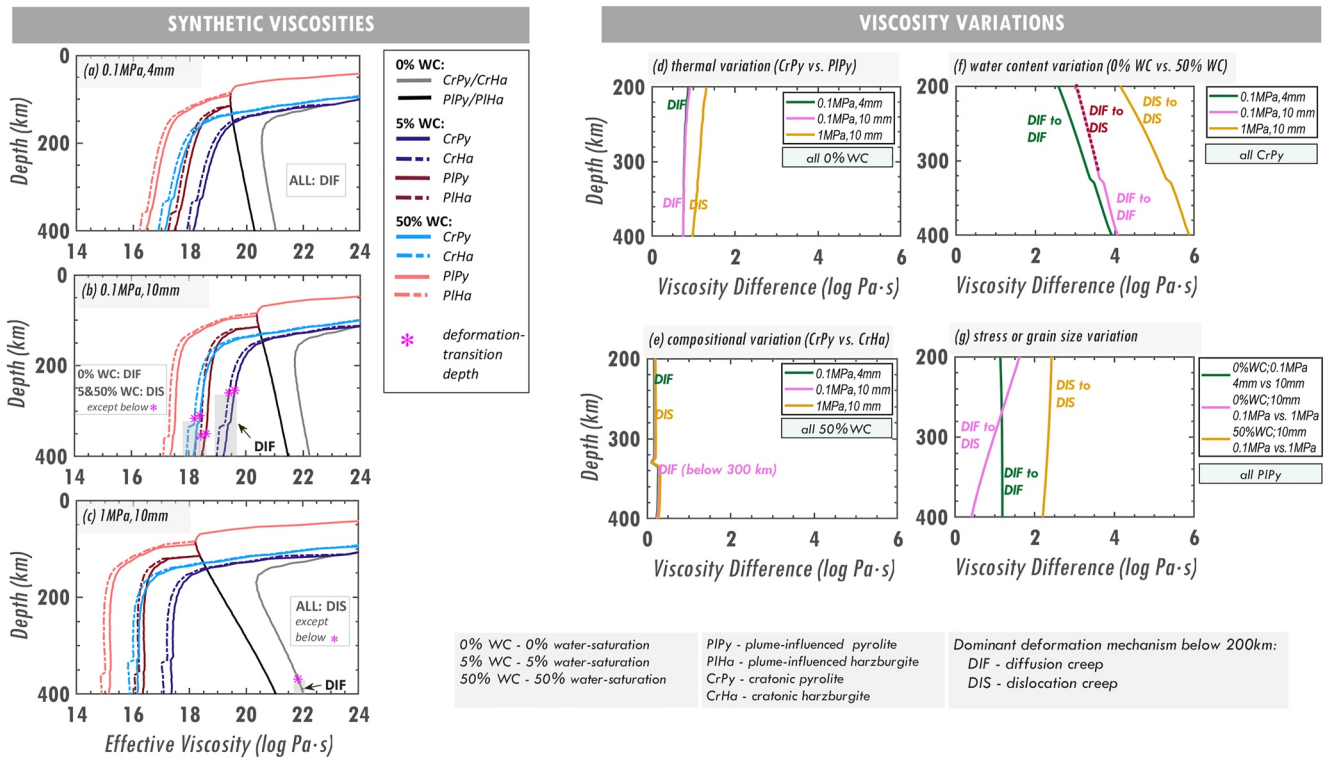
Figure 8. (a–c) Synthetic viscosities and (d–g) viscosity variations for harzburgite and pyrolite at different geotherms, water concentrations, stresses, and grain sizes. These viscosities are calculated using the geotherms and water concentrations in Figures 6c and 6d, respectively. For each panel in (a–c), three groups of viscosity structures can be identified based on their bulk water concentration: 0% WC, 5% WC, and 50% WC, where viscosities for 0% WC do not depend on composition (CrPy/CrHa and PlPy/PlHa pairs overlap). The dominant deformation mechanism below 200 km is included (see legend), where the synthetic viscosity structures in the same group (same bulk water) have the same deformation mechanism. All viscosities are produced by (a) diffusion creep at small stress and grain size, (b) varying mechanisms at small stress and large grain size, and (c) dislocation creep at relatively large stress and grain size. Differences between pairs of viscosity curves (d–g) show the relative effects of (d) thermal, (e) compositional, (f) water content, and (g) stress and grain size variations on viscosity. Mostly in panels (d–g), the dislocation regime produces the largest viscosity variation (in magnitude).

7.1. Forward Modeled Synthetic Viscosities

The modeled temperature, water content, stress, grain size and composition (particularly olivine proportion) heterogeneities in the upper mantle result in variations in viscosity (Figure 8). We consider different geotherms (cratonic and plume-influenced), water concentrations set to 0%, 5%, and 50% of water saturated conditions, stresses (0.1 and 1 MPa), grain sizes (4 and 10 mm), and compositions (harzburgite *Ha* and pyrolite *Py*) (Figures 8a–8c). At depths below 200 km, we identify the dominant deformation mechanism. The diffusion creep mechanism, which is dominant at small stresses, leads to increasing viscosity with depth for dry conditions because it is sensitive to increasing pressure. However, in wet conditions, diffusion creep leads to decreasing viscosity with depth due to its water sensitivity and because, in our compositions defined as 5% and 50% water saturated, water content increases with depth. In contrast, dislocation creep yields an approximately constant viscosity with depth for wet conditions because of the counter-balancing effects from pressure and water. This behavior is not evident in dry conditions, where viscosity increases significantly with depth due to the strong sensitivity of dislocation creep to pressure (Table 1).

Interestingly, for dry conditions (Figures 8a–8c, 0%WC) our calculations produce a low viscosity layer at the top of the asthenosphere without introducing composition or grain size variations across the lithosphere-asthenosphere boundary. Based on geophysical observations and experiments, this low viscosity layer, which may help to stabilize plate tectonics (e.g., Richards et al., 2001), has been attributed to partial melt (e.g., Chantel et al., 2016; Debayle et al., 2020; Selway & O'Donnell, 2019) or to solid-state mechanisms (e.g., Faul & Jackson, 2005) or to hydrogen content (Karato, 2012). Changes in composition such as these have not been tested in our models but
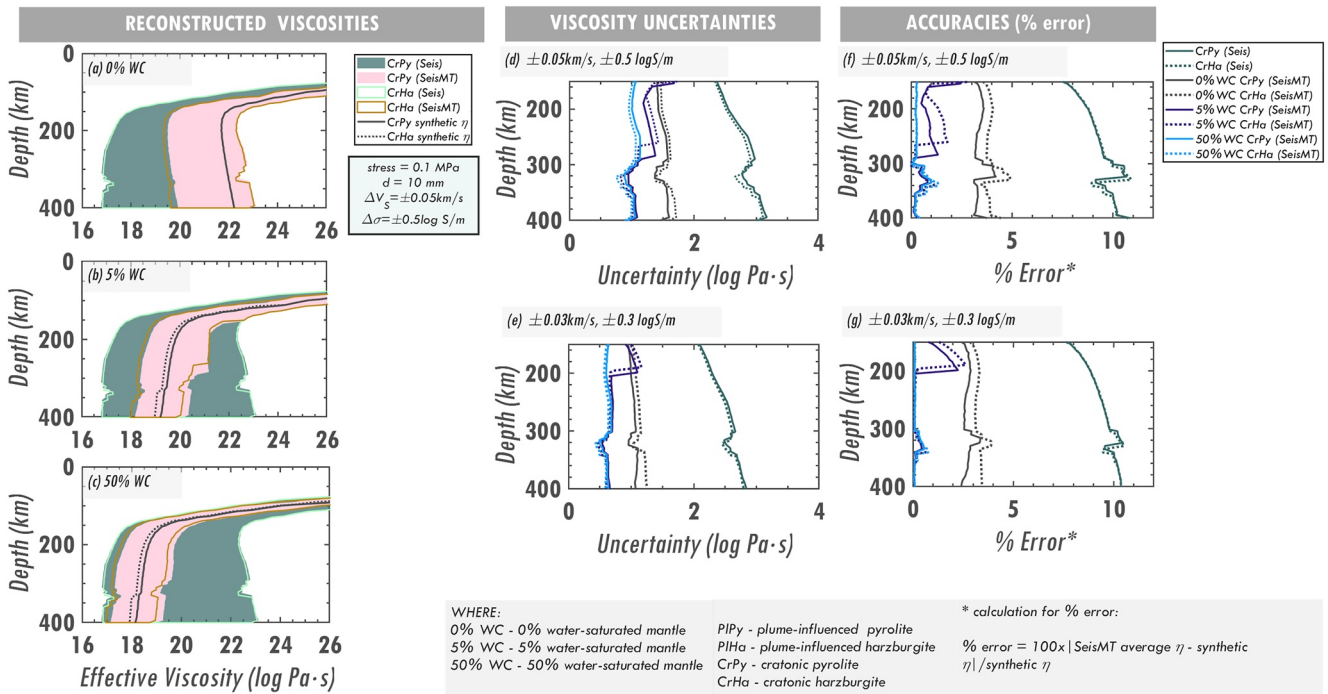
Figure 9. Reconstructed viscosities from seismics only, and both seismics and magnetotelluric constraints. We employ our method in constructing the viscosity structures (a–c) for different water concentrations (0%, 5%, and 50% WC) for cratonic harzburgite (CrHa) and pyrolite (CrPy) by utilizing the velocities and conductivities in Figures 6a and 6b, respectively. The compositional effect is evident, where inferred viscosities are slightly smaller for harzburgite than for pyrolite because it contains more water (a–c). We include different uncertainties on these modeled observations that result in viscosity ranges with different uncertainties (d and e). The viscosities reconstructed using only seismic constraints have large uncertainties (green lines in panels (d and e)) and are less accurate (f and g) because of unconstrained water.

our results show that for dehydrated upper mantle, the upper asthenosphere could have a low viscosity without needing to invoke compositional changes (e.g., Karato, 2012).

A 100 K temperature difference can produce about an order of magnitude viscosity variation (Figure 8d), while the presence of water (i.e., from 0% to 50% water saturation) can result in a larger change in viscosity (2–6 orders of magnitude, Figure 8f) that clearly emphasizes the need to constrain water in the upper mantle. Change in stress and/or grain size produces ∼0.5–2 orders of magnitude change in viscosity (Figure 8g). In contrast, a compositional change from pyrolite to harzburgite varies the viscosity by a factor of two (Figure 8e), which is measurable but not as big as the other factors. Apart from these factors, the dominant deformation mechanism can also impact the magnitude of the viscosity change, where the dislocation creep regime results in a larger viscosity variation compared to the diffusion creep regime (Figures 8d–8g).

7.2. Reconstructed Viscosities From Geophysical Observations

Commonly, we cannot unambiguously constrain the composition of the upper mantle using geophysical observations because the signal of composition trades off against other parameters like temperature, but instead we must refer to petrological studies. We also do not know the true geotherm. Many studies (e.g., Goes et al., 2000; Heeszel et al., 2016; Lucas et al., 2020; Milne et al., 2018) construct the thermal structure using seismics without accounting for variations in composition that could affect seismic velocities and therefore temperature and viscosity estimates. To investigate how compositional variations may impact viscosity estimates, we assume two known upper mantle compositions (harzburgite and pyrolite) in a cratonic setting. We reconstruct their synthetic viscosity structures at 0.1 MPa stress and 10 mm grain size using our developed method where their modeled seismic velocities (Figure 6a) and electrical conductivities (Figure 6b) are converted into temperatures and water concentrations, respectively (Figures 9a–9c). We consider the modeled electrical conductivities for 0%, 5%, and 50% of water saturation and infer these water concentrations and their associated uncertainties via MATE software. Figures 9a–9c shows the reconstructed viscosities that would be calculated if only seismic or if both

seismic and MT data were available, in comparison with the forward modeled synthetic viscosities. We consider different geophysical uncertainties ([0.05 km/s, 0.5 log S/m] and [0.03 km/s, 0.3 log S/m]) to assess their effect on viscosity estimates. From these assumptions, we evaluate the developed method by calculating how well both MT and seismics can constrain viscosity estimates (Figures 9d and 9e), and by calculating the accuracy of the reconstructed viscosities with respect to their synthetic viscosities (Figures 9f and 9g). We note again that, given the experimental and data uncertainties that cannot be quantified in this analysis, the absolute magnitudes of our results should be interpreted with caution, but the identified trends should be more robust and meaningful.

Viscosities reconstructed using only seismic constraints (Seis) have large uncertainties (Figures 9d and 9e) due to unconstrained water content. The viscosity uncertainties for pyrolite are larger than for harzburgite because the pyrolite model has slightly larger seismically-inferred temperature ranges (Figure B1, Appendix). When seismic models with smaller velocity uncertainties are available, viscosity uncertainties are reduced (Figure 9e).

When MT is integrated into our viscosity estimates (SeisMT), the uncertainties of the reconstructed viscosities are much reduced due to well-constrained water contents, and better represent the synthetic viscosities with high accuracy (Figures 9f and 9g). A composition change from pyrolite to harzburgite also affects viscosity uncertainty (compare solid and dashed lines, Figures 9d and 9e) due to variations in both water content and temperature ranges. Notably, increasing the bulk water content (say, from 0% to 50% WC) in harzburgite results in tighter viscosity estimates (by about an order of magnitude), because the MT interpretation shows unambiguously that the upper mantle is wet (Figure B1, Appendix) and thus increases the accuracy of our method. Furthermore, putting tighter bounds on both MT and seismic observations (small uncertainties) produces tighter viscosity estimates (at half an order of magnitude viscosity uncertainty reduction, Figure 9e) and improves the accuracy (Figure 9g) of our method.

8. Discussions

8.1. Limitations and Assumptions

In this theoretical investigation, we must select experimental models to convert MT and seismics to temperature and water content, and temperature, water, grain size and stress to viscosity. Although different experimental results exist and some results have significant uncertainties, in practice it has been necessary to select models (e.g., Table 1) in order to convert geophysical observations to mantle properties. Since experimental uncertainties for key parameters are often not measured or reported in the presentation of experimental results, and some significant sources of uncertainty (such as multiphase flow laws) have not yet been experimentally constrained, we do not include experimental uncertainties in our analysis (see Section 2). While this is a limitation, our method can easily be updated using new or different experimental results. In addition, the different mixing models (e.g., Archie's Law) employed in averaging electrical conductivities have their inherent limitations and assumptions that can also add uncertainties into the inferred temperature and water content. Averaging schemes for seismic velocities (Voigt-Reuss-Hill bounds) are unlikely to add significant uncertainty as their effects are smaller than experimental uncertainties (Stixrude & Lithgow-Bertelloni, 2005a, 2012). Where multiple experimental constraints exist, we have made conservative choices, including those used to calculate bulk conductivity (Table A1, Appendix) within MATE (Özaydin & Selway, 2020) and seismic velocities via Hacker and Abers (2004) and Stixrude and Lithgow-Bertelloni (2005b, 2011). Shear wave velocities computed with HeFESTo (Stixrude & Lithgow-Bertelloni, 2005b, 2011) are corrected for attenuation using the spherically averaged 1-D model QR19 (Romanowicz, 1995), which intrinsically includes the different sources of attenuation. Quantifying and propagating all the sources of error in experimental measurements is beyond the scope of this study and not really possible at this stage given the limitations on reporting and determination of uncertainties discussed in Section 2.

Current experimental data suggest that seismic attenuation is dependent on temperature, seismic frequency, melt and grain size (e.g., Chantel et al., 2016; Faul & Jackson, 2015), although precise experimental data quantifying these dependencies are challenging to collect and in some cases are still lacking. We have assumed a melt-free upper mantle for all our calculations, so we do not consider the impact of melt on attenuation. With regard to grain size, experimental data strongly suggest that attenuation due to elastically-accommodated grain boundary sliding increases with decreasing grain size (e.g., Jackson & Faul, 2010) but experiments do not yet accurately constrain the magnitude or frequency range of the associated attenuation peak or its pressure dependence. For this reason

we have instead modeled attenuation from seismic observations, without determining the source of attenuation. We do expect that attenuation should be larger for regions with smaller grain sizes at least over some upper mantle depth ranges. Our use of spherically averaged seismic models of attenuation (e.g., Dalton et al., 2008; Durek & Ekström, 1996; Korauglo & Romanowicz, 2018; Romanowicz, 1995) could limit spatial resolution and add uncertainty. Although attenuation amplitudes differ by <50% in these global averages, the same depth trends are evident in all models, particularly in the oceanic upper mantle (i.e., high attenuation in the LVZ, and then decreasing attenuation with increasing depth). Including the uncertainty of attenuation would add additional uncertainty to viscosity estimations based on seismically-inferred temperatures, but is likely to fall within the bounds of other sources of error. More important is to address the fact that seismic velocities are attenuated, by whichever mechanism provides the main source of attenuation and dispersion. Ignoring attenuation would wrongly lead us to estimate too-small viscosities associated with elevated temperatures inferred for a given seismic velocity.

We assume that viscosity flow laws for olivine represent the bulk upper mantle viscosity because olivine is the most abundant and well-studied mineral phase. However, the inherent viscosity of other phases such as pyroxenes (e.g., Chen et al., 2006) and the effect of different phases on the overall rheology (e.g., Bercovici & Skemer, 2017; Hansen & Warren, 2015; Tasaka et al., 2020; Warren & Hirth, 2006; N. Zhao et al., 2019) certainly place errors in this analysis. In principle, such uncertainty could be reduced by employing a viscosity law that incorporates multiple phases but such a flow law does not yet exist. For simplicity, our viscosity calculations are based on the experimental data summarized in Hirth and Kohlstedt (2003) and Ohuchi et al. (2015) and, apart from water, do not include the possible impact of trace and minor element compositions (e.g., Faul et al., 2016; Fei et al., 2013).

We assume three independent major deformation mechanisms in the upper mantle (diffusion creep, dislocation creep and DisGBS), which are assumed to control the effective viscosity calculation (Equation 2) as defined by Hirth and Kohlstedt (1996) for constant stress at any depth. We do not consider other mechanisms that may co-exist (i.e., Peierls mechanism which dominates at very high stresses (e.g., Kumamoto et al., 2017; Warren & Hirth, 2006)) or an overall mechanism (phase boundary sliding) that may control the bulk viscosity (N. Zhao et al., 2019). In principle, all of these factors (multiple phases, minor elements, and other deformation mechanisms) could be incorporated into a more general viscosity law, but the resulting viscosities would have correspondingly larger uncertainty.

Other plausible mantle compositions (e.g., lherzolite or MORB source) and the presence of melt are not considered here for simplicity but would affect seismic velocity, electrical conductivity and viscosity calculations. Also, since water transport into and out of the upper mantle is complicated (e.g., Karato et al., 2020; Peslier et al., 2017) and not well-constrained, we assume that bulk water content increases with depth in the upper mantle (e.g., Karato, 2012) instead of holding a constant value. Mixing and dehydration are also likely, leading to lateral variations in water content as interpreted from spatially varying conductivity signatures (e.g., Selway et al., 2019). This suggests that water in the upper mantle is heterogeneous, with potentially large lateral and radial viscosity variations (Figure 8f). Thus, we consider a simplified upper mantle with viscosities that are determined by assumed composition, geotherm, bulk water, stress, grain size, and geophysical uncertainties. Having good constraints on these parameters from geological and geophysical data will place tighter bounds on viscosity estimates (Figure 10).

Due to the assumptions and simplifications we have made, we are not making strict interpretations of our results, for instance, about the viscosity uncertainty reduction when MT is added into our analysis. Instead, we explore the factors that have the biggest impact on the viscosity estimates, and we calculate the resulting viscosity uncertainties and their variations due to the controlling factors, including the geophysical uncertainties. We mainly aim to provide a framework for estimating mantle viscosity using geophysical constraints. As mentioned, we have not propagated the experimental uncertainties associated with the laboratory-derived parameters into our results, partly because these uncertainties are not always consistently reported. Rock experiments are conducted under simplified and constrained conditions compared to the real Earth, and thus extrapolation to mantle conditions is required. Thus, incorporating experimental uncertainties into our analysis is a complex process that may result in misleading and erroneous uncertainty estimates. If estimates for some of these uncertainties existed, they could potentially be incorporated within our scheme, resulting in larger uncertainties for the geophysical parameters. Considering a varying and more realistic geophysical uncertainty along depth (which can be strongly dependent on the non-linear trend of the geophysical model) would affect the inferred viscosity structures in terms of magnitude and trend, and thus also the calculated viscosity uncertainties.
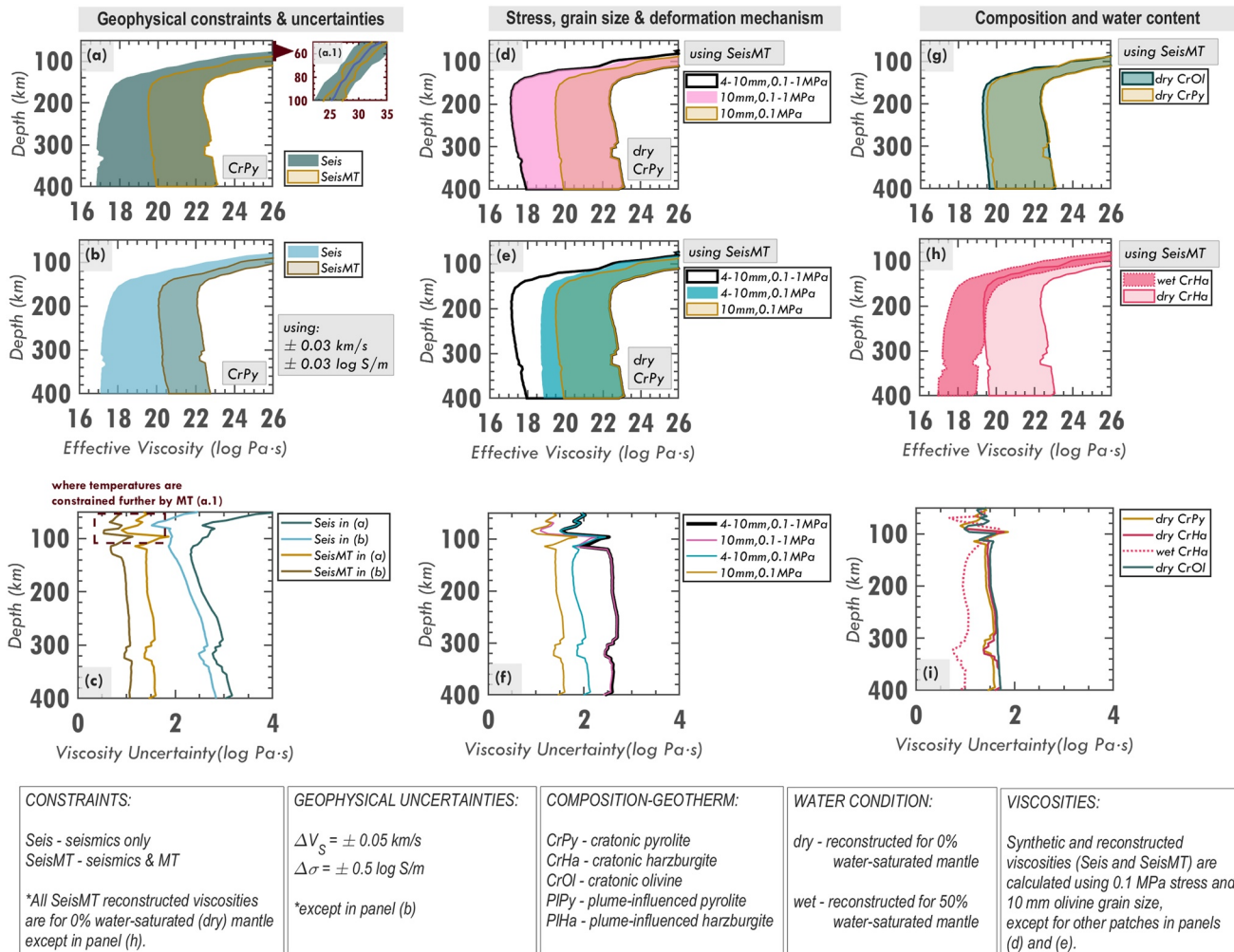
Figure 10. Factors affecting viscosity and its uncertainty. (a–c) Geophysical constraints and their uncertainties. We use a single choice for stress (0.1 MPa) and grain-size (10 mm) in calculating Seis and SeisMT viscosity bands in panels (a and b) for CrPy. Both seismic and magnetotelluric (MT) constraints improve bounds on the viscosity estimates, thus reducing viscosity uncertainties (brown/yellow lines in panel (c)), where seismics constrain temperature and MT constrains water. Improving MT and seismic data (e.g., from panels (b) to (c)) further reduces the viscosity uncertainties (brown line in panel (c)). (d–f) Stress, grain size, and deformation mechanism. All the reconstructed viscosities in panels (d and e) are SeisMT, where we assume different stress(es) and grain size(s) for dry CrPy: (black-edged patch) a range of grain-sizes (4–10 mm) and stresses (0.1–1 MPa), (pink patch) a range of stresses and a single choice for grain-size, (blue-green patch) a range of grain-sizes and a single choice for stress, and (yellow patch) a single choice for stress and grain-size. Using a single choice for stress and grain size constrains the viscosity estimates with smaller uncertainties, (yellow line, panel (f)) compared to using a wider range of stresses (pink line) and/or grain sizes (blue-green line). (g–i) Composition and water content. All the reconstructed viscosities in panels (g and h) are SeisMT using a single choice for stress (0.1 MPa) and grain-size (10 mm), but for different composition and water content: (yellow patch) dry CrPy, (green patch) dry CrOl, (light pink patch) dry CrHa, and (dark pink patch) wet CrHa. Variations in composition (green, pink, and yellow solid lines in panel (i)) produce variations in viscosity uncertainties, where knowing a composition apart from pure olivine reduces the viscosity uncertainty. Variations in bulk water content result in variations in viscosity uncertainty (pink solid and dotted lines).

8.2. Constraining Viscosity Estimates

8.2.1. Geophysical Constraints and Uncertainties

Using both MT and seismic constraints reduces the viscosity uncertainties (≥ 1.5 orders of magnitude; Figures 10a–10c) where the magnitude of reduction depends on the composition and water content (e.g., Figure 9d), and the geophysical uncertainties involved (Figure 10c). At shallow depths (<100 km; Figure 10a.1), the viscosities estimated from both seismics and MT data are more constrained than when using seismics alone because MT adds additional constraints on the temperature. If we cannot use both MT and seismic constraints (if they are incomptabile as in the "not possible" regions in Figures 3e–3i), we have to revisit the geophysical observations, experimental models, composition and other assumptions that we used.

8.2.2. Stress, Grain Size, and Deformation Mechanism

Constraining grain size and stress certainly improves viscosity estimates (Figures 10d–10f), and the viscosity magnitudes and uncertainties are controlled by the deformation mechanisms (e.g., there is large uncertainty in the dislocation creep regime). The viscosity uncertainty varies with depth or pressure when multiple deformation mechanisms occur in an upper mantle (Figure 10f) and is approximately constant when the upper mantle is deforming under a single mechanism. Hence, we can approximate how viscosity would change with depth if we know how the upper mantle is deforming. However, stress and grain size generally cannot be determined geophysically, so another tool that can provide us a hint about the mechanism would be beneficial. A potential tool for this is seismic anisotropy, which generally can be produced in the dislocation regime but not in the diffusion creep regime (e.g., Hansen et al., 2021), allowing us to distinguish whether the upper mantle is deforming under dislocation creep. This potentially provides information about the grain size that controls the anisotropic structure of the upper mantle by affecting the strain rates of diffusion and dislocation creep (e.g., Behn et al., 2009). However, it is difficult to constrain grain size geophysically because it evolves with time (e.g., Austin & Evans, 2007), and is affected by deformation history and temperature (e.g., Boneh & Skemer, 2014; Jackson et al., 2002, 2014). Recent developments in experimental measurements of attenuation by Jackson and Faul (2010) provide an insight on the effects of grain size on attenuation at seismic frequencies and approximately upper mantle temperatures, and provide a potential mechanism to constrain grain size from seismic attenuation measurements. As experimental data and attenuation measurements improve, estimates of upper mantle grain size and therefore viscosity are likely to become more accurate.

### 8.2.3. Composition, Temperature, and Water

Though composition is not empirically a controlling parameter in the viscosity flow laws we have used, we argue that it is also an important factor for calculating viscosities since it affects the conversion from seismic velocity to temperature and from electrical conductivity to water content (Section 6). Assuming a wrong composition (say pure olivine instead of pyrolite, Figure 10g) yields a discrepancy in viscosity estimates (Figure 10i). Even though the impact of composition on viscosity is much smaller than it is for parameters such as grain size and stress, the results shown here demonstrate that viscosity estimates from geophysical data will be improved if composition is considered (e.g., Ivins et al., 2022). Such discrepancies could be even larger for compositions with significantly less olivine than those considered in this study. Phase transitions also affect viscosity estimates where temperature and water content may change drastically (e.g., kinks in lines below 290 km, Figure 10i), which is not evident for a pure olivine assumption. Thus, any other constraints on composition (e.g., xenoliths) will certainly put tighter bounds on viscosity estimates.

As highlighted in previous sections, the calculated viscosity and its associated uncertainty depend on whether the mantle is wet or dry. Dry upper mantle is expected to be more viscous than wet upper mantle (Figure 10h) and may have larger uncertainties (Figure 10i). Apart from the viscosity reduction that occurs when water is introduced, the dominant deformation mechanism may also change, which can also affect the inferred viscosity uncertainties. Thus, even in situations where data uncertainties restrict the calculation of a specific water concentration, and where this restriction is exacerbated by disagreements between some olivine hydrous conductivity models, the general ability of MT to distinguish between a wet and dry upper mantle will provide a significant improvement to viscosity estimates.

Different geotherms produce different viscosity structures and may be associated with significantly different viscosity uncertainties. This variation in viscosity uncertainty may increase by changing the stress and grain size - that is by changing the dominant deformation mechanism (i.e., diffusion to dislocation). Given these observations, we can deduce that a mantle region that may be undergoing active deformation, with a hotter geotherm, smaller grain sizes, and relatively high stresses will have a larger viscosity uncertainty than a stable environment with a colder geotherm, lower stress and larger grain size (Figure 11).

9. Conclusions

We have developed a method that converts seismic and MT constraints into viscosity structures, accounting for possible compositional effects. Combining both geophysical constraints in viscosity calculations puts tighter bounds on the viscosity estimates compared to considering either one of them alone. Having good quality MT and seismic data with small uncertainties can further improve the viscosity estimates. MT can distinguish whether
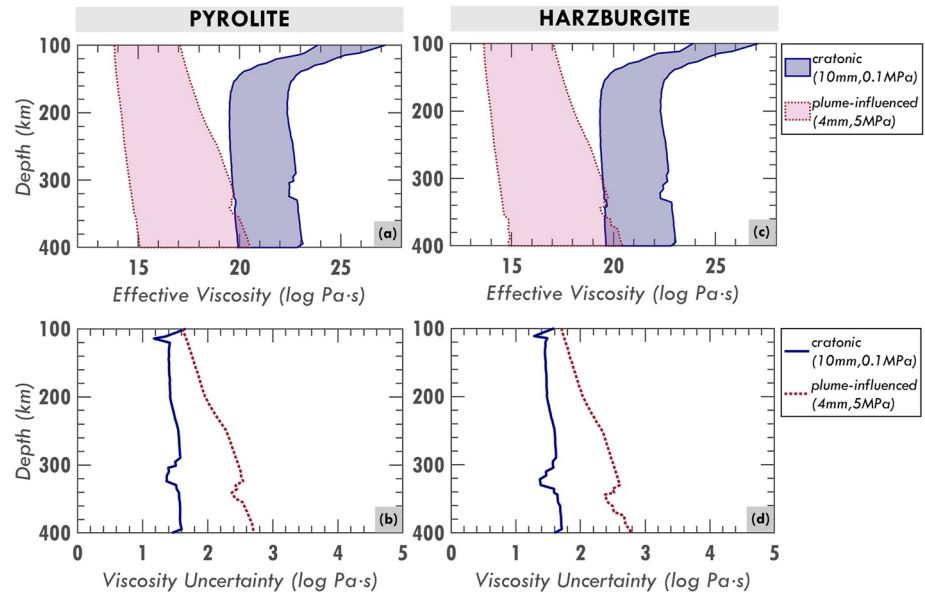
Figure 11. Viscosity estimates for the upper mantle in tectonically stable versus tectonically active environments. Viscosity structures (a and c) and their associated uncertainties (b and d) for tectonically active environments (hotter, "plume-influenced" geotherm) and tectonically stable environments (colder, "cratonic" geotherm), assuming pyrolite and harzburgite compositions, calculated at different grain size and stress combinations. We use the modeled seismic velocities (Figure 6a) and electrical conductivities for 0% WC (Figure 6b), and incorporate ±0.05 km/s and ±0.5 log S/m uncertainties, respectively. These geophysical models are converted into temperatures and water concentrations (Figure B1, Appendix) which are used to infer viscosity structures (a and c). The plume-influence case is assumed to be tectonically active, with smaller grain sizes (4 mm) and larger stresses (5 MPa) compared to the tectonically stable cratonic environment (10 mm and 0.1 MPa). Viscosity uncertainties are larger for the tectonically active environment, which is controlled by stress-sensitive dislocation creep.

an upper mantle is wet or dry, which greatly helps to reduce viscosity uncertainty. Thus, more MT surveys in environments where we want to have good viscosity structures (e.g., polar regions) would improve robust geodynamic and GIA modeling. For example, applying this method in places where currently only seismic observations are used (e.g., Heeszel et al., 2016; Lucas et al., 2020; Milne et al., 2018) would improve viscosity estimates. It could also be employed, for example, in Fennoscandia where viscosities are well constrained by GIA (e.g., Kierulf et al., 2014; Lambeck et al., 1998; Milne et al., 2001) to evaluate the viscosity structures obtained using this method. In addition, having a good knowledge of stress, grain size and composition can further improve the viscosity estimates (by more than an order of magnitude). Stress and grain size control the deformation regime (dislocation vs. diffusion creep, and grain-boundary sliding), which affects both the viscosity and its associated uncertainty. Composition directly affects seismic velocities and electrical conductivities, which are the constraints used in our method, and thus affects the output viscosities. For instance, we observe a trade-off between composition and temperature when estimating viscosity from seismic data. This can lead to an incorrect interpretation of both thermal and viscosity structures of mantle rocks if velocity variations are assumed to be only thermally controlled. Given these results, our method should help to improve estimates of mantle viscosity, and its uncertainty, for both tectonically active and stable environments (Figure 11), as long as the upper mantle is geophysically well-characterized by seismic and MT observations.

Appendix A: Geotherm Calculation

The constructed plume-influenced and cratonic geotherms (Figure 6c) represent two-end member cases that bracket a range of upper mantle states. The lithospheric component of both geotherms is calculated using Equation 4.31 of Turcotte and Schubert (2014), which is:

$$T_{\text{lith}}(z) = T_0 + \frac{q_m}{k} z + \frac{(q_m - q_0) h_r}{k} \left(1 - e^{-\frac{z}{h_r}} \right) \tag{A1}$$

where z is depth, $k = 3.35$ Wm^{-1}K^{-1} is the thermal conductivity, $h_r = 20$ km is the length scale for crustal radioactivity, q_0 is the surface heat flux and q_m is the mantle heat flux. The q_0 and q_m used for plume-influenced and cratonic geotherms are summarized in Table A1.

Table A1
Parameters Used in Constructing Different Geotherms and Models and Assumptions Used in Mantle Analysis Tool for Electromagnetics Software to Calculate Electrical Conductivity and Water

Parameters/Geotherm	Cratonic	Plume-influenced
T_p(°C)	1350	1450
q_m (mW/m^2)	30	70
q_0 (mW/m^2)	50	90
MATE entry	**Model**	
Composition entry:		
for Al$_2$O$_3$	*Calculated using* (Özaydin & Selway, 2020) $C_{al}^{opx} = 0.92654 + 4.69 \exp(-1.24012P)$	
Fe fractions	*0.10*	
Composition set-up:		
Al-dependency	*SAF Archon/Proton-Archon Xenoliths*	
Water Partitioning:	*Px handled independently*	
Opx/Ol	*Type 4—Demouchy 2017 average single value of opx/ol at 3 GPa and 1373 K with aluminous-opx-cpx-ol-gt assemblage*	
Cpx/Ol	*Type 5—Cpx-opx dependent cpx/ol values from P-dependent function*	
Water Solubility:		
Ol	*PadronNavarta2017*	
Conductivity Models:		
Ol	*Gardes2014*	
Opx	*Dai2009*	
Cpx	*Liu2019*	
Gt	*Dai2009a*	
Amp	*Hu2018H*	
Phlg	*Li2016*	

Below lithosphere, we define the mantle adiabat as:

$$T_{\mathrm{um}}(z) = T_p + \gamma z \tag{A2}$$

where T_p is the potential temperature of the adiabat at the surface (Table A1) and $\gamma = \left(\frac{\partial T}{\partial z}\right)_S$ is the adiabatic temperature gradient. We use $\gamma = 0.4$ K/km from Katsura et al. (2010).

We combine the above equations to form an overall geotherm using:

$$T(z) = \min(T_{\mathrm{lith}}, T_{\mathrm{um}}) - (200°\mathrm{C})\frac{300°\mathrm{C}}{300°\mathrm{C} + |T_{\mathrm{lith}} - T_{\mathrm{um}}|} \tag{A3}$$

where the (arbitrary) second term is included merely to smooth the transition between the two curves near their intersection.

Appendix B: Temperature and Water Content Inferred From Seismics and MT

We consider the forward-calculated shear wave velocities in Figure 6a for both harzburgite and pyrolite for plume-influenced and cratonic geotherms (Figure 6c) calculated in Section A. Then we attempt to reconstruct the thermal structures from the forward modeled shear wave velocities with the assumption that we know the compositions (harzburgite and pyrolite) and by assuming a constant velocity uncertainty along depth that translates
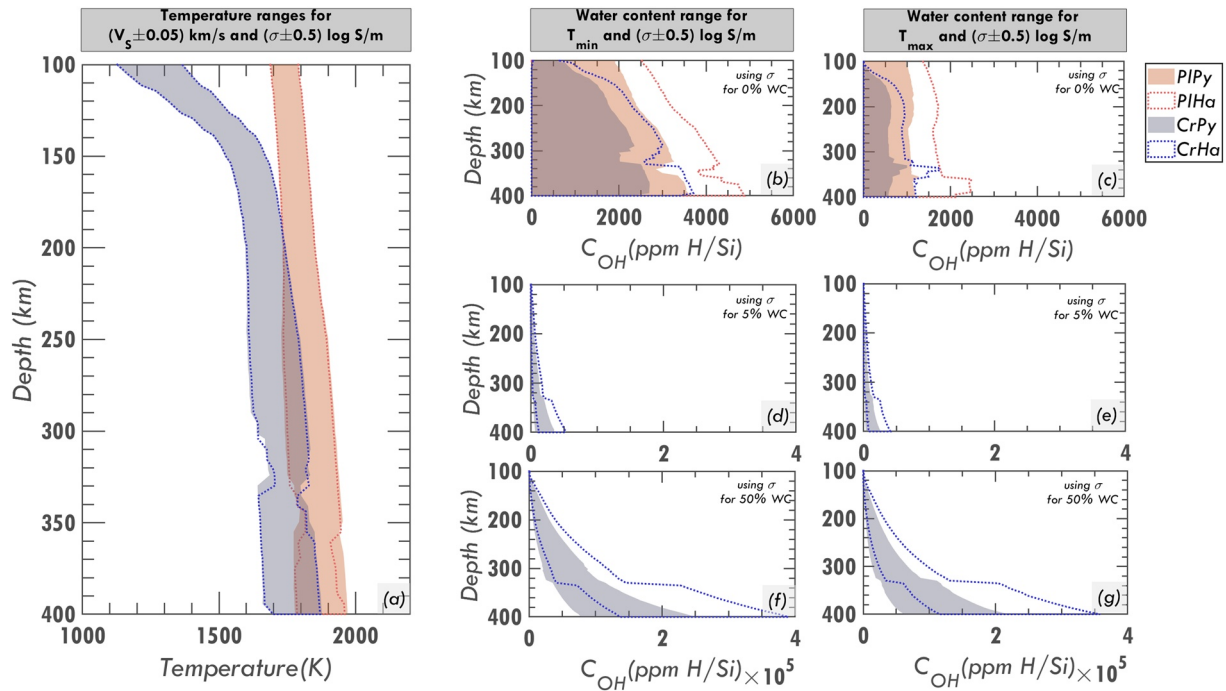
Figure B1. (a) Constrained temperatures and (b–g) water contents in olivine from seismic and magnetotelluric (MT) data. The velocity uncertainty (±0.05 km/s) used in the calculation translates into temperature uncertainty, producing a thermal structure with lower temperature bound (T_{min}) and upper temperature bound (T_{max}). The inferred thermal structures are further constrained when MT data is integrated (compare panel (a) with Figure 7b). From the electrical conductivity structures (with assumed ±0.5 log S/m uncertainty), the ranges of water content in olivine phase for harzburgite (dashed-edge colorless patches) and pyrolite (colored patches) are calculated for lower (b, d, and f) and upper temperature bounds (c, e, and g) using Mantle Analysis Tool for Electromagnetics software.

into temperature uncertainties (Figure B1a). Next, we try to determine the water contents (bulk and in olivine phase only) at depth using the inferred thermal structures and the forward-calculated electrical conductivities (Figure 6b) with constant uncertainty using the MATE software. To do this, we utilize the phase proportions (Figure 5) and the thermal structures as inputs into MATE. Then we uploaded into the MATE software the forward-modeled electrical conductivity structures (with uncertainty) assuming different bulk water contents (0%, 5%, and 50% WC) as synthetic MT data, and let the software solve for the water contents (Figures B1b–B1g) using the chosen models in Table A1. Due to the uncertainties included in this calculation, at any given temperature and depth, there is a range of water contents that can produce the desired conductivity range (as in Figure 2b). Thus, we need to determine the water content ranges for lower (b, d, and f) and upper (c, e, and g) temperature bounds separately. The seismically-inferred temperatures are constrained further by MT, particularly at shallow depths. Notably, the thermal structures for harzburgite are slightly tighter than those for pyrolite, but the water contents of harzburgite are significantly larger than pyrolite.

Data Availability Statement

The generated datasets are not archived in a repository since they are reproducible using the online softwares summarized in the Software Availability Statement. The thermodynamic simulation package HeFESTo (Stixrude & Lithgow-Bertelloni, 2005b, 2011) is available at https://github.com/stixrude/HeFESToRepository. The parameter set is at https://github.com/stixrude/HeFESTo_Parameters_251010. The MATE software (Özaydin & Selway, 2020) is available at https://github.com/sinanozaydin/MATE, and the models chosen are summarized in Table A1 (Appendix). The excel file of Hacker and Abers (2004) is in their supplementary information.

References

Artemieva, I. (2006). Global 1x1 thermal model TC1 for the continental lithosphere: Implications for lithosphere secular evolution. *Tectonophysics*, *416*(1–4), 245–277. https://doi.org/10.1016/j.tecto.2005.11.022

Austin, N. J., & Evans, B. (2007). Paleowattmeters: A scaling relation for dynamically recrystallized grain size. *Geology*, *35*(4), 343–346. https://doi.org/10.1130/g23244a.1

Ave Lallemant, H., Mercier, J.-C., Carter, N., & Ross, J. (1980). Rheology of the upper mantle: Inferences from peridotite xenoliths. *Tectonophysics*, *70*(1–2), 85–113. https://doi.org/10.1016/0040-1951(80)90022-0

Behn, M., Hirth, G., & Elsenbeck, J. R., II. (2009). Implications of grain size evolution on the seismic structure of the oceanic upper mantle. *Earth and Planetary Science Letters*, *282*(1–4), 178–189. https://doi.org/10.1016/j.epsl.2009.03.014

Bell, D. R., Rossman, G. R., Maldener, J., Endisch, D., & Rauch, F. (2003). Hydroxide in olivine: A quantitative determination of the absolute amount and calibration of the IR spectrum. *Journal of Geophysical Research*, *108*(B2), 2105. https://doi.org/10.1029/2001JB000679

Bercovici, D., & Ricard, Y. (2012). Mechanisms for the generation of plate tectonics by two-phase grain-damage and pinning. *Physics of the Earth and Planetary Interiors*, *202*, 27–55. https://doi.org/10.1016/j.pepi.2012.05.003

Bercovici, D., & Skemer, P. (2017). Grain damage, phase mixing and plate-boundary formation. *Journal of Geodynamics*, *108*, 40–55. https://doi.org/10.1016/j.jog.2017.05.002

Bina, C., & Helffrich, G. (1992). Calculation of elastic properties from thermodynamic equation of state principles. *Annual Review of Earth and Planetary Sciences*, *20*(1), 527–552. https://doi.org/10.1146/annurev.ea.20.050192.002523

Boneh, Y., & Skemer, P. (2014). The effect of deformation history on the evolution of olivine CPO. *Earth and Planetary Science Letters*, *406*, 213–222. https://doi.org/10.1016/j.epsl.2014.09.018

Chantel, J., Manthilake, G., Andrault, D., Novella, D., Yu, T., & Wang, Y. (2016). Experimental evidence supports mantle partial melting in the asthenosphere. *Science Advances*, *2*(5), e1600246. https://doi.org/10.1126/sciadv.1600246

Chen, S., Hiraga, T., & Kohlstedt, D. L. (2006). Water weakening of clinopyroxene in the dislocation creep regime. *Journal of Geophysical Research*, *111*(B8), B08203. https://doi.org/10.1029/2005JB003885

Connolly, J. A. D. (2005). Computation of phase equilibria by linear programming: A tool for geodynamic modeling and its application to subduction zone decarbonation. *Earth and Planetary Science Letters*, *236*(1–2), 524–541. https://doi.org/10.1016/j.epsl.2005.04.033

Conrad, C. P. (2013). The solid Earth's influence on sea level. *The Geological Society of America Bulletin*, *125*(7–8), 1027–1052. https://doi.org/10.1130/b30764.1

Conrad, C. P., & Hager, B. H. (1997). Spatial variations in the rate of sea level rise caused by the present-day melting of glaciers and ice sheets. *Geophysical Research Letters*, *24*(12), 1503–1506. https://doi.org/10.1029/97gl01338

Conrad, C. P., & Lithgow-Bertelloni, C. (2006). Influence of continental roots and asthenosphere on plate-mantle coupling. *Geophysical Research Letters*, *33*(5), 1–4. https://doi.org/10.1029/2005GL025621

Courtier, A., Bagley, B., & Revenaugh, J. (2007). Whole mantle discontinuity structure beneath Hawaii. *Geophysical Research Letters*, *34*(17), L17304. https://doi.org/10.1029/2007GL031006

Dalton, C. A., & Ekström, G. (2006). Global models of surface wave attenuation. *Journal of Geophysical Research*, *111*(B5), B05317. https://doi.org/10.1029/2005JB003997

Dalton, C. A., Ekström, G., & Dziewonski, A. M. (2008). The global attenuation structure of the upper mantle. *Journal of Geophysical Research*, *113*(B9), B09303. https://doi.org/10.1029/2007JB005429

Debayle, E., Bodin, T., Durand, S., & Ricard, Y. (2020). Seismic evidence for partial melt below tectonic plates. *Nature*, *586*(7830), 555–559. https://doi.org/10.1038/s41586-020-2809-4

Durek, J., & Ekström, G. (1996). A radial model of anelasticity consistent with long-period surface-wave attenuation. *Bulletin of the Seismological Society of America*, *86*, 144–158. https://doi.org/10.1785/BSSA08601A0144

Faul, U., Cline II, C., David, E., Berry, A., & Jackson, I. (2016). Titanium-hydroxyl defect-controlled rheology of the Earth's upper mantle. *Earth and Planetary Science Letters*, *452*, 227–237. https://doi.org/10.1016/j.epsl.2016.07.016

Faul, U., & Jackson, I. (2005). The seismological signature of temperature and grain size variations in the upper mantle. *Earth and Planetary Science Letters*, *234*(1–2), 119–134. https://doi.org/10.1016/j.epsl.2005.02.008

Faul, U., & Jackson, I. (2015). Transient creep and strain energy dissipation: An experimental perspective. *Annual Review of Earth and Planetary Sciences*, *43*(1), 541–569. https://doi.org/10.1146/annurev-earth-060313-054732

Fei, H., Wiedenbeck, M., Yamazaki, D., & Katsura, T. (2013). Small effect of water on upper-mantle rheology based on silicon self-diffusion coefficients. *Nature*, *498*(7453), 213–215. https://doi.org/10.1038/nature12193

Fullea, J., Lebedev, S., Martinec, Z., & Celli, N. L. (2021). WINTERC-G: Mapping the upper mantle thermochemical heterogeneity from coupled geophysical-petrological inversion of seismic waveforms, heat flow, surface elevation and gravity satellite data. *Geophysical Journal International*, *226*(1), 146–191. https://doi.org/10.1093/gji/ggab094

Gardés, E., Gaillard, F., & Tarits, P. (2014). Toward a unified hydrous olivine electrical conductivity law. *Geochemistry, Geophysics, Geosystems*, *15*(12), 4984–5000. https://doi.org/10.1002/2014GC005496

Glover, P. W. (2010). A generalized Archie's law for n phases. *Geophysics*, *75*(6), E247–E265. https://doi.org/10.1190/1.3509781

Goes, S., Govers, R., & Vacher, P. (2000). Shallow mantle temperatures under Europe from P and S wave tomography. *Journal of Geophysical Research*, *105*(B5), 11153–11169. https://doi.org/10.1029/1999jb900300

Hacker, B., & Abers, G. (2004). Subduction Factory 3: An Excel worksheet and macro for calculating the densities, seismic wave speeds, and H2O contents of minerals and rocks at pressure and temperature. *Geochemistry, Geophysics, Geosystems*, *5*(1), Q01005. https://doi.org/10.1029/2003GC000614

Hansen, L., Faccenda, M., & Warren, J. (2021). A review of mechanisms generating seismic anisotropy in the upper mantle. *Physics of the Earth and Planetary Interiors*, *313*, 106662. https://doi.org/10.1016/j.pepi.2021.106662

Hansen, L., & Warren, J. (2015). Quantifying the effect of pyroxene on deformation of peridotite in a natural shear zone. *Journal of Geophysical Research: Solid Earth*, *120*(4), 2717–2738. https://doi.org/10.1002/2014JB011584

Heeszel, D., Wiens, D. W., Anandakrishnan, S., Aster, R., Dalziel, I., Huerta, A., et al. (2016). Upper mantle structure of central and West Antarctica from array analysis of Rayleigh wave phase velocities. *Journal of Geophysical Research: Solid Earth*, *121*(3), 1758–1775. https://doi.org/10.1002/2015JB012616

Hirth, G., & Kohlstedt, D. (1996). Water in the oceanic upper mantle: Implications for rheology, melt extraction and the evolution of the lithosphere. *Earth and Planetary Science Letters*, *144*(1–2), 93–108. https://doi.org/10.1016/0012-821x(96)00154-9

Hirth, G., & Kohlstedt, D. (2003). Rheology of the upper mantle and the mantle wedge: A view from the experimentalists. *Inside the Subduction Factory, Geophysical Monograph*, *138*, 83–105.

Ita, J., & Stixrude, L. (1992). Petrology, elasticity, and composition of the mantle transition zone. *Journal of Geophysical Research*, *97*(B5), 6849–6866. https://doi.org/10.1029/92JB00068

Ivins, E. R., & Sammis, C. G (1995). On lateral viscosity contrast in the mantle and the rheology of low-frequency geodynamics. *Geophysical Journal International*, *123*(2), 305–322. https://doi.org/10.1111/j.1365-246x.1995.tb06856.x

Ivins, E. R., van der Wal, W., Wiens, D. A., Lloyd, A. J., & Caron, L. (2022). Antarctic upper mantle rheology. In A. P. Martin & W. van der Wal (Eds.), *The Geochemistry and Geophysics of the Antarctic mantle* (Vol. 56). Geological Society. https://doi.org/10.1144/M56-2020-19

Jackson, I., & Faul, U. (2010). Grainsize-sensitive viscoelastic relaxation in olivine: Towards a robust laboratory-based model for seismological application. *Physics of the Earth and Planetary Interiors*, *183*(1–2), 151–163. https://doi.org/10.1016/j.pepi.2010.09.005

Jackson, I., Faul, U., & Skelton, R. (2014). Elastically accommodated grain-boundary sliding: New insights from experiment and modeling. *Physics of the Earth and Planetary Interiors*, *228*, 203–210. https://doi.org/10.1016/j.pepi.2013.11.014

Jackson, I., Fitz Gerald, J., Faul, U., & Tan, B. (2002). Grain-size-sensitive seismic wave attenuation in polycrystalline olivine. *Journal of Geophysical Research*, *107*(B12), 2360. https://doi.org/10.1029/2001JB001225

Jacobsen, S. D., Jiang, F., Mao, Z., Duffy, T. S., Smyth, J. R., Holl, C. M., & Frost, D. J. (2008). Effects of hydration on the elastic properties of olivine. *Geophysical Research Letters*, *35*(14), L14303. https://doi.org/10.1029/2008GL034398

Johnston, P., Wu, P., & Lambeck, K. (1998). Dependence of horizontal stress magnitude on load dimension in glacial rebound models. *Geophysical Journal International*, *132*(1), 41–60. https://doi.org/10.1046/j.1365-246x.1998.00387.x

Karaoglu, H., & Romanowicz, B. (2018). Inferring global upper-mantle shear attenuation structure by waveform tomography using spectral element method. *Geophysical Journal International*, *213*(3), 1536–1558. https://doi.org/10.1093/gji/ggy030

Karato, S.-I. (2012). On the origin of asthenosphere. *Earth and Planetary Science Letters*, *321*, 95–103. https://doi.org/10.1016/j.epsl.2012.01.001

Karato, S.-I., & Jung, H. (2003). Effects of pressure on high-temperature dislocation creep in olivine. *Philosophical Magazine*, *83*(3), 401–414. https://doi.org/10.1080/0141861021000025829

Karato, S.-I., & Karki, B. (2001). Origin of lateral variation of seismic wave velocities and density in the deep mantle. *Journal of Geophysical Research*, *106*(B10), 21771–21783. https://doi.org/10.1029/2001jb000214

Karato, S.-I., Karki, B., & Park, J. (2020). Deep mantle melting, global water circulation and its implications for the stability of the ocean mass. *Progress in Earth and Planetary Science*, *7*(1), 76. https://doi.org/10.1186/s40645-020-00379-3

Katsura, T., Yoneda, A., Yamazaki, D., Yoshino, T., & Ito, E. (2010). Adiabatic temperature profile in the mantle. *Physics of the Earth and Planetary Interiors*, *183*(1–2), 212–218. https://doi.org/10.1016/j.pepi.2010.07.001

Kaufmann, G., & Lambeck, K. (2000). Mantle dynamics, postglacial rebound and the radial viscosity profile. *Physics of the Earth and Planetary Interiors*, *121*(3–4), 301–324. https://doi.org/10.1016/s0031-9201(00)00174-6

Khan, S. A., Sasgen, I., Bevis, M., van Dam, T., Bamber, J., Wahr, J., et al. (2016). Geodetic measurements reveal similarities between post-Last Glacial Maximum and present-day mass loss from the Greenland ice sheet. *Science Advances*, *2*(9), e1600931. https://doi.org/10.1126/sciadv.1600931

Kierulf, H., Steffen, H., Simpson, M., Lidberg, M., Wu, P., & Wang, H. (2014). A GPS velocity field for Fennoscandia and a consistent comparison to glacial isostatic adjustment models. *Journal of Geophysical Research: Solid Earth*, *119*(8), 6613–6629. https://doi.org/10.1002/2013JB010889

Kumamoto, K., Thom, C., Wallis, D., Hansen, L., Armstrong, D., Warren, J., et al. (2017). Size effects resolve discrepancies in 40 years of work on low-temperature plasticity in olivine. *Science Advances*, *3*(9), e1701337. https://doi.org/10.1126/sciadv.1701338

Lambeck, K., Smither, C., & Johnston, P. (1998). Sea-level change, glacial rebound and mantle viscosity for northern Europe. *Geophysical Journal International*, *134*(1), 102–144. https://doi.org/10.1046/j.1365-246x.1998.00541.x

Lebedev, S., Boonen, J., & Trampert, J. (2009). Seismic structure of Precambrian lithosphere: New constraints from broad-band surface-wave dispersion. *Lithos*, *109*(1–2), 96–111. https://doi.org/10.1016/j.lithos.2008.06.010

Lee, C.-T. A. (2003). Compositional variation of density and seismic velocities in natural peridotites at STP conditions: Implications for seismic imaging of compositional heterogeneities in the upper mantle. *Journal of Geophysical Research*, *108*(B9), 2441. https://doi.org/10.1029/2003JB002413

Liu, L., & Hasterok, D. (2016). High-resolution lithosphere viscosity and dynamics revealed by magnetotelluric imaging. *Science*, *353*(6307), 1515–1519. https://doi.org/10.1126/science.aaf6542

Lloyd, A. J., Wiens, D. A., Nyblade, A. A., Anandakrishnan, S., Aster, R. C., Huerta, A. D., et al. (2015). A seismic transect across West Antarctica: Evidence for mantle thermal anomalies beneath the Bentley Subglacial Trench and the Marie Byrd Land Dome. *Journal of Geophysical Research: Solid Earth*, *120*(12), 8439–8460. https://doi.org/10.1002/2015JB012455

Lucas, E., Soto, D., Nyblade, A. A., Lloyd, A., Aster, R., Wiens, D., et al. (2020). P- and S-wave velocity structure of central West Antarctica: Implications for the tectonic evolution of the West Antarctic Rift System. *Earth and Planetary Science Letters*, *546*, 116437. https://doi.org/10.1016/j.epsl.2020.116437

Mei, S., & Kohlstedt, D. L. (2000). Influence of water on plastic deformation of olivine aggregates: 1. Diffusion creep regime. *Journal of Geophysical Research*, *105*(B9), 21457–21469. https://doi.org/10.1029/2000jb900179

Milne, G., Davis, J., Mitrovica, J., Scherneck, H.-G., Johansson, J., Vermeer, M., & Koivula, H. (2001). Space-geodetic constraints on glacial isostatic adjustment in Fennoscandia. *Science*, *291*(5512), 2381–2385. https://doi.org/10.1126/science.1057022

Milne, G., Latychev, K., Schaeffer, A., Crowley, J., Lecavalier, B., & Audette, A. (2018). The influence of lateral Earth structure on glacial isostatic in Greenland. *Geophysical Journal International*, *214*(2), 1252–1266. https://doi.org/10.1093/gji/ggy189

Mitrovica, J., & Forte, A. (1997). Radial profile of mantle viscosity: Results from the joint inversion of convection and postglacial rebound observables. *Journal of Geophysical Research*, *102*(B2), 2751–2769. https://doi.org/10.1029/96jb03175

Mitrovica, J., Tamisiea, M., Davis, J., & Milne, G. (2001). Recent mass balance of polar ice sheets inferred from patterns of global sea-level change. *Nature*, *409*(6823), 1026–1029. https://doi.org/10.1038/35059054

Naif, S. (2018). An upper bound on the electrical conductivity of hydrated oceanic mantle at the onset of dehydration melting. *Earth and Planetary Science Letters*, *482*, 357–366. https://doi.org/10.1016/j.epsl.2017.11.024

O'Donnell, J., Selway, K., Nyblade, A., Brazier, R., Wiens, D., Anandakrishnan, S., et al. (2017). The uppermost mantle seismic velocity and viscosity structure of central West Antarctica. *Earth and Planetary Science Letters*, *472*, 38–49. https://doi.org/10.1016/j.epsl.2017.05.016

Ohuchi, T., Kawazoe, T., Higo, Y., Funakoshi, K.-I., Suzuki, A., Kikegawa, T., & Irifune, T. (2015). Dislocation-accommodated grain boundary sliding as the major deformation mechanism of olivine in the Earth's upper mantle. *Science Advances*, *1*(9), 1–10. https://doi.org/10.1126/sciadv.1500360

Özaydin, S., & Selway, K. (2020). MATE: An analysis tool for the interpretation of magnetotelluric models of the mantle. *Geochemistry, Geophysics, Geosystems*, *21*(9), 1–26. https://doi.org/10.1029/2020GC009126

Padrón-Navarta, J., & Hermann, J. (2017). A subsolidus olivine water solubility equation for the Earth's upper mantle. *Journal of Geophysical Research: Solid Earth*, *122*(12), 9862–9880. https://doi.org/10.1002/2017JB014510

Paulson, A., Zhong, S., & Wahr, J. (2005). Modelling post-glacial rebound with lateral viscosity variations. *Geophysical Journal International*, *163*(1), 357–371. https://doi.org/10.1111/j.1365-246X.2005.02645.x

Paulson, A., Zhong, S., & Wahr, J. (2007). Limitations on the inversion for mantle viscosity from postglacial rebound. *Geophysical Journal International*, *168*(3), 1195–1209. https://doi.org/10.1111/j.1365-246X.2006.03222.x

Peltier, W. (2004). Global glacial isostasy and the surface of the ice-age Earth: The ICE-5G (VM2) model and GRACE. *Annual Review of Earth and Planetary Sciences*, *32*(1), 111–149. https://doi.org/10.1146/annurev.earth.32.082503.144359

Peltier, W., Farrell, W., & Clark, J. (1978). Glacial isostasy and relative sea level: A global finite element model. *Tectonophysics*, *50*(2–3), 81–110. https://doi.org/10.1016/0040-1951(78)90129-4

Peslier, A., Schönbächler, M., Busemann, H., & Karato, S.-I. (2017). Water in the Earth's interior: Distribution and origin. *Space Science Reviews*, *212*(1–2), 743–810. https://doi.org/10.1007/s11214-017-0387-z

Pollitz, F., Banerjee, P., Grijalva, K., Nagarajan, B., & Bürgmann, R. (2008). Effect of 3-D viscoelastic structure on post-seismic relaxation from the 2004 M=9.2 Sumatra earthquake. *Geophysical Journal International*, *173*(1), 189–204. https://doi.org/10.1111/j.1365-246X.2007.03666.x

Richards, M. A., Yang, W.-S., Baumgardner, J. R., & Bunge, H.-P. (2001). Role of a low-viscosity zone in stabilizing plate tectonics: Implications for comparative terrestrial planetology. *Geochemistry, Geophysics, Geosystems*, *2*(8), 1026. https://doi.org/10.1029/2000GC000115

Romanowicz, B. (1995). A global tomographic model of shear attenuation in the upper mantle. *Journal of Geophysical Research*, *100*(B7), 12375–12394. https://doi.org/10.1029/95jb00957

Selway, K., & O'Donnell, J. (2019). A small unextractable melt fraction as the cause for the low velocity zone. *EPSL*, *517*, 117–124. https://doi.org/10.1016/j.epsl.2019.04.012

Selway, K., O'Donnell, J. P., & Özaydin, S. (2019). Upper mantle melt distribution from petrologically constrained magnetotellurics. *Geochemistry, Geophysics, Geosystems*, *20*(7), 3328–3346. https://doi.org/10.1029/2019GC008227

Selway, K., Smirnov, M., Beka, T., O'Donnell, J., Minakov, A., Senger, K., Faleide, J. I., & Kalscheuer, T. (2020). Magnetotelluric constraints on the temperature, composition, partial melt content, and viscosity of the upper mantle beneath svalvard. *Geochemistry, Geophysics, Geosystems*, *21*, 1–12. https://doi.org/10.1029/2020GC008985

Shen, W., Wiens, D., Anandakrishnan, S., Aster, R., Gerstoft, P., Bromirski, P., et al. (2018). The crust and the upper mantle structure of central and West Antarctica from Bayesian inversion of Rayleigh wave and receiver functions. *Journal of Geophysical Research: Solid Earth*, *123*(9), 7824–7849. https://doi.org/10.1029/2017JB015346

Stevens, N., Parizek, B., & Alley, R. (2016). Enhancement of volcanism and geothermal heat flux by ice-age cycling: A stress modeling study of Greenland. *Journal of Geophysical Research: Earth Surface*, *121*(8), 1456–1471. https://doi.org/10.1002/2016JF003855

Stixrude, L., & Lithgow-Bertelloni, C. (2005a). Mineralogy and elasticity of the oceanic upper mantle: Origin of the low-velocity zone. *Journal of Geophysical Research*, *110*(B3), B03204. https://doi.org/10.1029/2004JB002965

Stixrude, L., & Lithgow-Bertelloni, C. (2005b). Thermodynamics of mantle minerals - I. Physical properties. *Geophysical Journal International*, *162*(2), 610–632. https://doi.org/10.1111/j.1365-246X.2005.02642.x

Stixrude, L., & Lithgow-Bertelloni, C. (2011). Thermodynamics of mantle minerals - II. Phase equilibria. *Geophysical Journal International*, *184*(3), 1180–1213. https://doi.org/10.1111/j.1365-246X.2010.04890.x

Stixrude, L., & Lithgow-Bertelloni, C. (2012). Geophysics of chemical heterogeneity in the mantle. *Annual Review of Earth and Planetary Sciences*, *40*(1), 569–595. https://doi.org/10.1146/annurev.earth.36.0310207.124244

Tasaka, M., Zimmerman, M. E., & Kohlstedt, D. L. (2020). Rheological weakening of olivine + orthopyroxene aggregates due to phase mixing: Effects of orthopyroxene volume fraction. *Journal of Geophysical Research: Solid Earth*, *125*(9), e2020JB019888. https://doi.org/10.1029/2020JB019888

Turcotte, D., & Schubert, G. (2014). *Geodynamics* (3rd edn.). Cambridge University Press.

Wang, D., Mookherjee, M., Xu, Y., & Karato, S. (2006). The effect of water on the electrical conductivity of olivine. *Nature*, *443*(26), 977–980. https://doi.org/10.1038/nature05256

Wang, K., Hu, Y., & He, J. (2012). Deformation cycles of subduction earthquakes in a viscoelastic Earth. *Nature*, *484*(7394), 327–332. https://doi.org/10.1038/nature11032

Warren, J., & Hirth, G. (2006). Grain size sensitive deformation mechanisms in naturally deformed peridotites. *Earth and Planetary Science Letters*, *248*(1–2), 438–450. https://doi.org/10.1016/j.epsl.2006.06.006

Xu, W., Lithgow-Bertelloni, C., Stixrude, L., & Ritsema, J. (2008). The effect of bulk composition and temperature on mantle seismic structure. *Earth and Planetary Science Letters*, *275*(1–2), 70–79. https://doi.org/10.1016/j.epsl.2008.08.012

Yoshino, T., Matsuzaki, T., Shatskiy, A., & Katsura, T. (2009). The effect of water on the electrical conductivity of olivine aggregates and its implications for the electrical structure of the upper mantle. *Earth and Planetary Science Letters*, *288*(1–2), 291–300. https://doi.org/10.1016/j.epsl.2009.09.032

Zhao, N., Hirth, G., Cooper, R., Kruckenberg, S., & Cuckjati, J. (2019). Low viscosity of mantle rocks linked to phase boundary sliding. *EPSL*, *517*, 83–94. https://doi.org/10.1016/j.epsl.2019.04.019

Zhao, Y.-H., Ginsberg, S. B., & Kohlstedt, D. L. (2004). Solubility of hydrogen in olivine: Dependence on temperature and iron content. *Contributions to Mineralogy and Petrology*, *147*(2), 155–161. https://doi.org/10.1007/s00410-003-0524-4